

**EFFECT OF THERMOMECHANICAL TREATMENT ON DYNAMIC STRAIN  
AGING AND MICROSTRUCTURAL EVOLUTION IN  
18 Ni 250 MARAGING STEEL**

*by*

**BALAJI SUNDARAM**

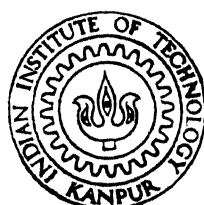
ME

1991

M

SUN

EFF



DEPARTMENT OF METALLURGICAL ENGINEERING

**INDIAN INSTITUTE OF TECHNOLOGY KANPUR**

MAY, 1991

EFFECT OF THERMOMECHANICAL TREATMENT ON DYNAMIC STRAIN AGING AND  
MICROSTRUCTURAL EVOLUTION IN 18 Ni 250 MARAGING STEEL

A Thesis Submitted  
In Partial Fulfilment of the Requirements  
for the Degree of  
MASTER OF TECHNOLOGY

by  
BALAJI SUNDARAM

to the  
DEPARTMENT OF METALLURGICAL ENGINEERING  
INDIAN INSTITUTE OF TECHNOLOGY, KANPUR

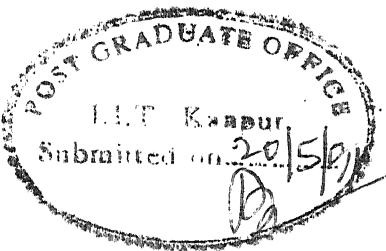
May 1991

ME-1991-m-SUN-EFF

99 DEC 1991

CENTRAL LIBRARY  
I.I.T. KANPUR  
Acc. No. A. 332498

C E R T I F I C A T E



It is certified that the work contained in the thesis entitled "Effect of Thermomechanical Treatment on Dynamic Strain Aging and Microstructural Evolution in 18 Ni 250 Maraging Steel" by "Balaji Sundaram" , has been carried out under our supervision and that this work has not been submitted elsewhere for a degree.

*S. Bhargava*  
Assistant Professor

Dr S. Bhargava

*M.L. Vaidya*  
Professor

Dr M.L. Vaidya

Department of Metallurgical Engineering  
Indian Institute of Technology, Kanpur

May 1991

## CONTENTS

	PAGE NO.
ACKNOWLEDGEMENTS	vi
LIST OF TABLES	vii
LIST OF FIGURES	x
LIST OF SYMBOLS	xiv
LIST OF ABBREVIATIONS	xvi
ABSTRACT	xvii
 Chapter 1      Introduction	 1
1.1      Characteristic properties of maraging steels	2
1.2      Applications	3
1.3      Phase transformations in maraging steels	3
1.3.1      Martensite formation	3
1.3.2      Morphological features of martensite in maraging steels	4
1.3.3      Austenite Reversion	6
A. Diffusion-Assisted Austenite Reversion	7
B. Diffusionless austenite reversion	8
1.3.4      Aging behaviour and kinetics	10
1.4.1      Conventional heat treatment of maraging steels	12
1.4.2      Unconventional heat treatment of maraging steels	13
1.5      Dynamic strain aging of 18 Ni 250 maraging steels	14
1.5.1      Phenomenology	15
1.5.2      Physical processes that cause serrated flow	16
 Chapter 2      Aim of the Present Work	 18

Chapter 3	Experimental Procedres	19
3.1	Material	19
3.2	Thermomechanical treatment	19
3.3	Heat treatment	20
3.4	Dynamic strain aging tests	20
3.4.1	The Tensile test	20
3.4.2	Measurement of stress decrement vs strain rate	21
3.4.3	Calculation of activation energy	22
3.5	Microscopy	22
3.5.1	Optical Microscopy	23
3.5.2	Scanning electron microscopy	23
3.5.3	Transmission Electron Microscopy	24
Chapter 4	Results and Discussion	25
4.1	Dynamic strain aging behaviour of maraging steels	25
4.1.1	Dynamic strain aging behaviour of double solutionized samples without subjecting them to thermomechanical treatment.	25
4.1.2	Dynamic strain aging behaviour of samples that have been subjected to thermomechanical treatment followed by double solutionizing	29
4.1.3	Models for dynamic strain aging	31
4.2	Microstructures of 18 Ni 250 maraging steels	33
4.2.1	Microstructures of batch 1 specimens	33
4.2.2	Microstructures of batch 2 specimens	34

		V
Chapter 5	Conclusions and Suggestions for Further Work	95
5.1	Conclusions	95
5.2	Suggestions for further work	96
REFERENCES		97
APPENDIX-1	Expression for the activation energy, $\Delta H$	101
APPENDIX-2	Significance of stress decrement, $\sigma_D$	104

## ACKNOWLEDGEMENTS

I am highly indebted to Prof M.L. Vaidya and Dr S. Bhargava for suggesting this thought provoking and fascinating topic for my project work. Their incisive analysis, keen insight and subtle suggestions in the various intricacies of the project enabled me to emerge triumphant in this endeavour.

I wish to place on record my deep sense of gratitude to the Chairman, Dept of Metallurgical Engineering and the esteemed faculty of the department for graciously extending the laboratory facilities for conducting my investigation.

My heart felt thanks are due to the following persons : Mr K.P. Mukherjee for helping me in metallography; Mr M.N. Mungole for helping me in electrolytic etching; Mr H.C. Srivastava for helping me during heat treatment; Mr G.R. Hoshing for the excellent typing of the manuscript and to all other final year M.Tech. students who in some measure or the other contributed to the success of my project. Last but not the least, I wish to thank the workshop staff for rendering help during specimen preparation and heat treatment.

BALAJI SUNDARAM

## LIST OF TABLES

TABLE	TITLE	PAGE NO.
1.1	Nominal chemical composition and strengths of common maraging steels	70
1.2	Comparison of embrittlement resistance of maraging steel with carbon and alloy steel	71
3.1	Chemical composition of 18 Ni 250 maraging steel	72
3.2	Rolling schedule	73
3.3	Tensile test parameters	74
3.4	Various etchants and their chemical composition used for metallographic studies in 18% Ni maraging steel	75
4.01	Variation of stress decrement, $\sigma_D$ as a function of $\log \dot{\epsilon}$ at $286^{\circ}\text{C}$ (ARB2+TMT+DS)	76
4.02	Variation of stress decrement, $\sigma_D$ as a function of $\log \dot{\epsilon}$ at $350^{\circ}\text{C}$ (ARB2+TMT+DS)	77
4.03	Variation of stress decrement, $\sigma_D$ as a function of $\log \dot{\epsilon}$ at $400^{\circ}\text{C}$ (ARB2+TMT+DS)	78
4.04	Variation of $\log \dot{\epsilon}$ as a function of $\frac{1}{T} \times 10^3$ at $\sigma_D = 130 \text{ MPa}$ (ARB2+TMT+DS)	79
4.05	Variation of stress decrement, $\sigma_D$ and critical strain, $\epsilon_c$ as a function of XV at $286^{\circ}\text{C}$ (ARB1+DS)	80
4.06	Variation of stress decrement, $\sigma_D$ and critical strain, $\epsilon_c$ as a function of XV at $350^{\circ}\text{C}$ (ARB1+DS)	81

4.07	Variation of stress decrement, $\sigma_D$ and critical strain, $\epsilon_c$ as a function of XV at $400^{\circ}\text{C}$ (ARB1+DS)	82
4.08	Variation of $\log \dot{\epsilon}$ as a function of $\frac{1}{T} \times 10^3$ at $\sigma_D = 130 \text{ MPa}$ (ARB1+DS)	83
4.09	Variation of stress decrement, $\sigma_D$ as a function of $\log \dot{\epsilon}$ at $286^{\circ}\text{C}$ (ARB1+DS)	84
4.10	Variation of stress decrement, $\sigma_D$ as a function of $\log \dot{\epsilon}$ at $350^{\circ}\text{C}$ (ARB1+DS)	85
4.11	Variation of stress decrement, $\sigma_D$ as a function of $\log \dot{\epsilon}$ at $400^{\circ}\text{C}$ (ARB1+DS)	86
4.12	Variation of stress decrement, $\sigma_D$ and critical strain, $\epsilon_c$ as a function of temperature at $\text{XV} = 5 \text{ mm/min}$ (ARB2+TMT+DS)	87
4.13	Variation of stress decrement, $\sigma_D$ and critical strain, $\epsilon_c$ as a function of temperature at $\text{XV} = 1 \text{ mm/min}$ (ARB2+TMT+DS)	88
4.14	Variation of stress decrement, $\sigma_D$ and critical strain, $\epsilon_c$ as a function of temperature at $\text{XV} = .5 \text{ mm/min}$ (ARB2+TMT+DS)	89
4.15	Variation of stress decrement, $\sigma_D$ and critical strain, $\epsilon_c$ as a function of temperature at $\text{XV} = 10 \text{ mm/min}$ (ARB2+TMT+DS)	90
4.16	Variation of stress decrement, $\sigma_D$ and critical strain, $\epsilon_c$ as a function of XV at $286^{\circ}\text{C}$ (ARB2+TMT+DS)	91

4.17 Variation of stress decrement,  $\sigma_D$  and critical strain,  $\epsilon_c$  as a function of XV at  $350^{\circ}\text{C}$  (ARB2+TMT+DS)

92

4.18 Variation of stress decrement,  $\sigma_D$  and critical strain,  $\epsilon_c$  as a function of XV at  $400^{\circ}\text{C}$  (ARB2+TMT+DS)

93

4.19 Effect of heat treatment and thermomechanical treatment on grain size.

94

## LIST OF FIGURES

FIGURE	TITLE	PAGE NO.
1.1	Iron-rich portion of the iron-nickel equilibrium diagram	36
1.2	Metastable iron-nickel diagram	37
1.3	Schematic illustration showing the construction of lath martensite structure in a prior austenite grain.	38
1.4	Schematic illustrations showing the morphological characteristics of lath martensite structure in .2 % C steel and 18 % Ni maraging steel	39
1.5	Structure change of reversed austenite with holding (austenitzing) temperature and holding time in 18 % Ni maraging steel (heating rate : 100 <sup>0</sup> C/min), solution treated specimen	40
1.6	Specific heat versus temperature curves of the ternary and quaternary alloys : Heating rate is about 0.025 K/s	41
1.7	Change in the packet size and block width of lath martensite with the prior austenite grain size in Fe-0.2 % C alloy and 18 % Ni maraging steel	42
1.8	Change in the ratio of G.S. (Prior austenite grain size) to P.S. (Packet size of lath martensite) with the prior austenite grain	

size in Fe-0.2% C alloy and 18 % Ni maraging steel	43
3.1 Temperature-time diagram showing thermomechanical treatment	44
3.2 Electrolytic etching apparatus	45
3.3 Standard dimensions of the tensile test specimen	46
3.4 Schematic plot of load vs elongation	47
3.5 Schematic plot of stress decrement, $\sigma_D$ as a function of strain rate, $\dot{\epsilon}$ at different temperatures	48
3.6 Schematic plot of $\log \dot{\epsilon}$ as a function of reciprocal of temperature at constant stress decrement, $\sigma_{D_1}$	49
4.01 Variation of load with elongation (ARB1+DS)	50
4.02 Variation of stress decrement, $\sigma_D$ at 8.3% strain as a function of strain rate, $\dot{\epsilon}$ at different temperatures (ARB1+DS)	51
4.03 Variation of flow stress, $\sigma$ at 2% strain as a function of strain rate $\dot{\epsilon}$ at different temperatures (ARB1+DS)	52
4.04 Variation of strain rate, $\dot{\epsilon}$ as a function of temperature at constant stress decrement, $\sigma_D$ (ARB1+DS)	53
4.05 Variation of critical strain, $\epsilon_c$ as a function of strain rate, $\dot{\epsilon}$ , at different temperatures (ARB1+DS)	54

4.06	Variation of load with elongation (TMT+DS)	55
4.07	Schematic plot of variation of stress with elongation (TMT/TMT+SS/TMT+DS)	56
4.08	Variation of first critical strain, $\epsilon_{c_1}$ , as a function of strain rate, $\dot{\epsilon}$ at different temperatures (TMT+DS)	57
4.09	Variation of load with elongation (TMT+DS)	58
4.1	Variation of stress decrement, $\sigma_D$ at 9.4% strain as a function of strain rate, $\dot{\epsilon}$ at different temperatures (TMT+DS)	59
4.11	Variation of strain rate, $\dot{\epsilon}$ as a function of temperature at constant stress decrement, $\sigma_D$ (TMT+DS)	60
4.12	ARB1, 500X, EE	61
4.13	ARB1, 5000X, EE	61
4.14	ARB1, 500X, CE	61
4.15	ARB1+SS, 500X, EE	61
4.16	ARB1+SS, 500X, CE	62
4.17	ARB1+DS, 500X, EE	62
4.18	ARB1+DS, 1000X, EE	62
4.19	ARB1+DS, 200X, CE	62
4.20	ARB1+DS, 500X, CE	63
4.21	ARB1, 100,000X, TEM	63
4.22	ARB2, 500X, EE	63
4.23	ARB2, 500X, CE	63
4.24	ARB2+SS, 500X, EE	64
4.25	ARB2+SS, 500X, CE	64

4.26	ARB2+DS, 500X, EE	64
4.27	ARB2+DS, 500X, CE	64
4.28	ARB2+TMT, 200X, EE	65
4.29	ARB2+TMT, 500X, EE	65
4.30	ARB2+TMT, 1000X, EE	65
4.31	ARB2+TMT, 500X, EE	65
4.32	ARB2+TMT, 2000X, EE	66
4.33	ARB2+TMT, 5000X, EE	66
4.34	ARB2+TMT, 500X, CE	66
4.35	ARB2+TMT, 1000X, CE	66
4.36	ARB2+TMT, 4000X, CE	67
4.37	ARB2+TMT+SS, 200X, EE	67
4.38	ARB2+TMT+SS, 500X, CE	67
4.39	ARB2+TMT+SS, 1000X, CE	67
4.40	ARB2+TMT+DS, 500X, EE	68
4.41	ARB2+TMT+DS, 500X, CE	68
4.42	ARB2+TMT+DS, 1000X, CE	68
4.43	ARB2+TMT, $170 \times 10^3$ X, TEM	68
4.44	ARB2+TMT+DS, $80 \times 10^3$ X, TEM	69
4.45	ARB2+TMT+DS, 4000X, CE	69

## LIST OF SYMBOLS

$\sigma$	Stress
$\sigma_D$	Stress decrement
$\epsilon$	True strain
$e$	Engineering strain
T	Temperature ( $^{\circ}$ K)
$\dot{\epsilon}$	True strain rate
$\dot{\epsilon}_p$	plastic strain rate
$\dot{\epsilon}_e$	Elastic strain rate
$\epsilon_c$	Critical strain
$\rho_m$	Mobile dislocation density
$b$	Burgers vector
$v$	Dislocation velocity
$t_w$	Waiting time
$t_f$	Flight time
$\ell$	Distance between obstacles
$\rho_f$	Forest dislocation density
$\Delta H$	Activation energy
$\epsilon_{c_1}$	First critical strain
$\sigma_{D_1}$	Stress decrement for first stage/domain of serrated yielding
$\sigma_{D_2}$	Stress decrement for second stage of serrated yielding
$\gamma$	Surface energy
$\dot{\sigma}$	Stress rate
$\Delta G$	Change in Gibbs free energy of the system
A	Overall frequency factor

$\Delta S$	Change in entropy of the system
$\bar{\sigma}$	Effective stress
$\sigma_\mu$	Long range internal stress field at any given structure
R	Gas constant
$\alpha$	Ferrite
$\alpha'$	Martensite
$\gamma$	Austenite

## LIST OF ABBREVIATIONS

ARB1	As Received Batch 1
SS	Single solutionized
DS	Double solutionized
TMT	Thermomechanical treatment
ARB2	As Received Batch 2
XV	Cross head velocity
EE	Electrolytically etched
CE	Chemically etched
TEM	Transmission Electron Micrograph

**ABSTRACT**

The dynamic aging of 18 Ni 250 maraging steel was investigated. The activation energy for thermomechanically and heat treated samples was found to be  $\sim 1.24$  eV. A number of models have been suggested to explain the phenomenon of dynamic strain aging. Two new models involving twinning and short range order have been suggested in the light of previous investigations and the experimental results obtained from the present investigation.

Microstructural observations were carried out to investigate the effect of thermomechanical treatment on the microstructural features of 18 Ni 250 maraging steel.

## CHAPTER I

### INTRODUCTION

Maraging steels are ultra high strength steels generally containing nickel, molybdenum, cobalt, titanium, aluminium and a very low percentage of carbon [ $C \leq 0.03\%$ ]. The strengthening effect during aging of these steels is caused by the precipitation of intermetallic phases based on substitutional alloying elements within the matrix of iron-nickel martensite [1]. The term 'maraging' is an abbreviation of 'martensite age hardening'. Precipitates which form in maraging steels are based on intermetallic compositions and are not carbides as in HSLA steels. Hence carbon in maraging steels is treated as an impurity and is kept at the lowest possible concentration. Carbon, if present, causes embrittlement of the steel by forming titanium carbides or carbonitrides [1].

Compositions of common grades of maraging steels are given in table 1.1. Yield strength of maraging steels varies from 1030 to 2420 MPa (150 to 350 ksi). Some experimental [1] maraging steels have yield strength as high as 3450 MPa (500 ksi).

The use of intermetallic precipitates to achieve strengthening provides several unique characteristics to maraging steel that set them apart from conventional steels. Since there is no [2] pinning of dislocations by carbon, toughness is enhanced. Hardenability is of no concern because of high Ni content and low carbon content. Further, the low carbon martensite formed during cooling from the austenitic phase field is relatively soft, about 30 to 35 HRC. During age hardening there is only a very slight dimensional change. Thus fairly

intricate shapes can be machined in [3] soft condition and then hardened with minimum of distortion.

### 1.1 Characteristic Properties of Maraging Steels

1. The chief property making maraging steels so interesting as a structural material is their excellent [1] combination of strength and fracture toughness.

2. Maraging steels possess reasonably good mechanical properties at elevated as well as at low temperatures. Although the fracture toughness values ( $K_{IC}$ ) sometimes decreases by ~ 60% when the temperature is lowered from room temperature to  $-194^{\circ}\text{C}$ , the combination of strength with toughness is [1] still rather good over a wide range of low temperatures which makes these steels highly attractive for cryogenic applications. The high temperature capability of these steels is generally limited to  $480^{\circ}\text{C}$ .

3. The fatigue properties of these steels are generally comparable to those of high strength alloyed steels.

4. 18 Ni maraging steels generally offer better threshold plane strain stress intensity values ( $K_{ISCC}$ ) than other high strength steels. In terms of critical crack size, maraging steels can tolerate larger flaws without experiencing crack propagation.

5. Embrittlement resistance of maraging steels when compared to that of plain carbon and alloy steels is generally found to be superior. Some of the typical features of maraging steels in this regard have been shown in Table 1.2. [2].

## 1.2 Applications

The uses of conventional 18% Ni maraging steels can be classified into three major groups

- (a) Hydrospace, aeronautical and aerospace applications- rocket motor cases, torsion bar suspensions for space vehicles, parts of missile engines, aircraft landing gear components, submergence marine vehicles for great depths etc.
- (b) Structural and machine components - pressure vessels, bolts, fasteners, springs, barrels for rapid firing guns, fuel injection pumps, etc.
- (c) Tools - diecasting dies, moulds for plastic industry, some cold forming dies, etc. [1].

## 1.3 PHASE TRANSFORMATIONS IN MARAGING STEELS

### 1.3.1 Martensite Formation

As mentioned earlier, maraging steels derive their ultra-high strength from a structure which consists of a martensite matrix having uniformly distributed fine precipitates of intermetallic phases.

The formation of martensite in maraging steels can be directly related to the iron-rich end of the Fe-Ni phase diagram which is shown in Figure 1.1. The low temperature equilibrium phases in the Fe rich alloys are either ferrite (at concentrations of < 10 wt% Ni) or ferrite and austenite (at concentrations of 10 wt% < Ni < 33 wt%). Above ~ 33 wt% of Ni only austenite is present at room temperature.

Detailed studies on Fe-Ni alloys, however, reveal that a surprising variety of transformation reactions can take place in

4

these alloys [1]. In the range of 0-5 wt% Ni alloys, ferrite forms independent of the cooling rate. In alloys containing 5-10 wt% Ni, ferrite forms when the transformation is carried out at slower cooling rate but with an increase in cooling rate the transformation product becomes martensite instead of ferrite. Increasing Ni content further lowers the cooling rate necessary to form martensite [1].

Therefore, in maraging steels, which contain ~ 18 wt% Ni, high temperature austenitic phase does not transform into equilibrium phases as predicted by the Fe-Ni phase diagram (Figure 1.1). Instead even at slow cooling rate austenite transforms to martensite which has a bcc structure. The martensite start temperature,  $M_s$ , in Fe-Ni alloys depends on the Ni content of the alloy - the higher the Ni content lower is the  $M_s$  temperature.

There exists a 'thermal hysteresis' in Fe-Ni alloys between the formation of martensite on cooling and its reversion to austenite on heating [4]. This thermal hysteresis is depicted in Figure 1.2. Due to relatively higher Ni content and low carbon content in maraging steels, their hardenability is generally independent of cooling rate and the alloys are usually cooled in air.

### 1.3.2 Morphological Features of Martensite in Maraging Steels

Martensites in Fe - 10-25% Ni alloys possess the lath morphology. Martensites in alloys containing > 25 wt% Ni have been found to have 'twinned' structure. The precise conditions that determine whether lath or twinned martensite is formed are still uncertain, but two factors seems to play a dominant role viz

the  $M_s$  temperature and stacking fault energy. A decrease in  $M_s$  temperature and an increase in stacking fault energy (SFE) favour the formation of twinned martensite [1]. The  $M_s$  temperature can be modified either by changes in the composition or by plastic deformation while the SFE varies only as a result of alloying.

The orientation relationship between martensite platelets and austenite matrix has been suggested to be Kurdiumov-Sachs (K-S) [1].

$$\left. \begin{array}{l} (111)_{\gamma} \parallel (011)_{\alpha'}, \\ [1\bar{1}0]_{\gamma} \parallel [1\bar{1}1]_{\alpha'} \end{array} \right\} \text{[K-S]}$$

The simultaneous existence of the Kurdiumov-Sacks and the Nishiyama-Wasserman (N-W) orientation relationships has also been reported [3].

$$\left. \begin{array}{l} (111)_{\gamma} \parallel (011)_{\alpha'}, \\ [100]_{\gamma} \parallel [100]_{\alpha'} \end{array} \right\} \text{[N-W]}$$

Morphology and microstructures of lath martensites in Fe-Ni alloys and maraging steels have been studied by Marder and Marder [5] and Maki et al. [6] respectively. It has been shown that the microstructure of lath martensite is characterized by packets and blocks, which are composed of laths, in the original austenite grain as shown in Figure 1.3. Thus a prior austenite grain, during its martensitic transformation, gets partitioned into several packets (marked as A in Figure 1.3). Each packet is further subdivided into blocks (marked as B in Figure 1.3). Packets consist of parallel laths with the same habit plane. Each block is made up of a matrix of martensite laths having

essentially the same variant, namely the identical orientation and the identical habit plane. The blocks are separated from one another by high angle boundaries [5].

Maki et al.[6] have shown that packets and blocks in martensites of 18% maraging steels are clearly defined. Morphological features studied on coarse prior austenite grain size maraging steel samples (grain size varying from 59-445  $\mu\text{m}$ ) revealed that blocks were parallel and well defined and were extended almost throughout the packet. These features are in contrast to morphology of lath martensites formed in low carbon ( $\text{C} \leq 0.2 \text{ wt\%}$ ) steels where blocks of martensite do not develop distinctly and are generally wedge shaped and often segmented. A schematic diagram showing morphological features in low carbon and maraging steel martensites is shown in Figure 1.4.

### 1.3.3 Austenite Reversion

As indicated by the Fe-Ni phase diagram (Figures 1.1 and 1.2), the iron-nickel martensites are metastable and can revert to ferrite or/and austenite. The austenite reversion, i.e., reaction involving  $\alpha' \longrightarrow \gamma$  transformation, depending on the chemical composition of the maraging steel and the transformation temperature, can be slow or rapid. The slow transformation involves redistribution of constituent elements, i.e. it is diffusion assisted, and results in a characteristic 'stripe' pattern having austenite layers separated by regions of ferrite [7]. On the other hand, rapid reversion involves martensitic transformation mechanism, i.e. it is diffusionless shear type of transformation.

### A. Diffusion-Assisted Austenite Reversion

Metastable martensite can decompose by a diffusion controlled reaction to ferrite and austenite after prolonged holding at temperatures below austenite start temperature ( $A_s$ ). Depending on the temperature and composition the austenite thus formed may become so rich in Ni that its  $M_s$  temperature lies below the ambient temperature. As a result retained austenite may often be found in the microstructures of maraging steels. The rate of austenite reversion reaction depends on temperature and, fortunately for maraging steels, this rate at temperatures of the order of  $485^\circ$  (the typical aging temperature) is slow enough so that precipitation hardening can be achieved before the reversion reaction predominates.

The rate of austenite reversion is also quite sensitive to composition. In binary iron-nickel alloys increasing nickel levels generally tends to accelerate austenite formation [3]. In steels containing other alloying elements the effect of individual elements will partly depend on whether the element is an austenite or ferrite stabiliser. A much stronger effect probably results from change in matrix composition that accompanies precipitation. Titanium, for example, has been found to markedly retard reversion, evidently because the formation of  $Ni_3Ti$  lowers the nickel content of the matrix [1]. Molybdenum additions, on the other hand enhance reversion [1]. In this case the austenite reversion has been suggested to be associated with the dissolution of  $Ni_3Mo$  and the formation of  $Fe_2Mo$  presumably, when  $Ni_3Mo$  goes into solution causing the local enrichment of the matrix with

nickel favouring the reversion process.

In binary alloys of Fe-Ni the austenite reversion reaction has been suggested [8] to be a one step process while in more complex alloys it has been found to be occurring by two successive steps. Austenite reversion has generally been found to occur at the boundaries of the martensite platelets (packets, blocks or laths).

### B. Diffusionless Austenite Reversion

Austenite can also be formed by heating the martensite above the  $A_s$  temperature. In this case the transformation from martensite to austenite is by shear and the resultant austenite has the same chemical composition as that of the initial martensite. Crystallographically this transformation is similar to the austenite to martensite transformation.

Austenite reversion in 18% Ni maraging steels has been studied by Hosomi et al. [9] and Maki et al. [6]. Maki et al. obtained austenite start,  $A_s$ , and austenite finish,  $A_f$  temperatures of 18% Ni maraging steel containing ~ 9 wt% Co, 5 wt% Mo and 0.7 wt% Ti by resistivity change measurements.  $A_s$  and  $A_f$  for this steel were found to be  $684^{\circ}\text{C}$  and  $786^{\circ}\text{C}$  respectively.

Microstructural examination of transformed structure in all the cases showed that the location of the reversed austenite grain boundaries exactly corresponded to the prior austenite grain boundaries of the original specimen and hence there was no change in austenite grain size by the  $\alpha' \rightarrow \gamma$  reverse transformation. Retention of the grain size in reverted austenite has also been reported by other workers [10] and has sometimes been referred to

as the microstructural memory effect'. It has been suggested that the propensity for structure inheritance depends on a number of factors namely [11]

- i) alloying elements
- ii) plastic deformation imparted to the material prior to its transformation
- iii) heating rate
- iv) volume effect of the  $\alpha' \rightarrow \gamma$  transformation.

Sadovskiy et al. have shown that retained austenite does not have a decisive role in the microstructural memory effect [7]. For example distinct structural inheritance was observed in maraging steels with or without the presence of retained austenite.

Further, it has been observed that the reversed austenite, right after the completion of  $\alpha' \rightarrow \gamma$  transformation is unrecrystallized irrespective of holding temperature. With an increase in holding time or in holding temperature, the reversed austenite changes from the unrecrystallized to the recrystallized austenite. Because of the recrystallization of the reversed austenite, the austenite grain size becomes fine, and then increases with an increase in holding temperature due to the grain growth.

In the case of Fe-30 ~ 34% Ni alloys in which  $\alpha' \rightarrow \gamma$  reverse transformation takes place at fairly low temperatures by the mechanism of shear transformation, the recrystallization of reversed austenite occurs by further heating because of a high density of lattice defects caused by shear mechanism of martensitic reverse transformation [12,13]. In contrast to Fe-30 ~ 34% Ni alloys, austenite reversion in maraging steels, has

been suggested to be occurring partly by the diffusional process in addition to the shear mechanism because of their high  $A_s$  and  $A_f$  temperatures. Recrystallization behaviour of reversed austenite in 18% Ni maraging steel has been schematically shown in figure 1.5.

Sadovskiy et al have shown that in 18% Ni maraging steels austenite reversion can occur during heating in three distinct ways [7]:

- (i) by the appearance of plate like nuclei of austenite of one orientation which merge together during further growth and secure reconstruction of the prior austenite grain.
- (ii) by means of nucleation of equiaxed austenite in addition to plate-like austenite.
- (iii) by means of oriented formation of infrafath nuclei of austenite of several orientations.

These orientations are related to the initial  $\alpha'$  by martensite orientation relationships. When phase transformation is complete this kind of nucleation mechanism does not result in the recovery of the prior austenite grain, but in the appearance of a group of fine grains which are in specific orientation relation with the original  $\alpha'$  grain. This mechanism therefore does not contradict the general observation of structural inheritance in maraging steels.

#### 1.3.4. Aging Behaviour and Kinetics

After transformation to martensite most maraging steels are aged for 3 to 5 hours in the temperature range of  $480^{\circ}\text{C}$  -  $500^{\circ}\text{C}$ . Two main processes [1] leading to hardening may occur during aging

(a) Precipitation of various intermetallic compounds, sometimes preceded by the formation of thermodynamically metastable intermediate phases.

(b) Ordering in Co-containing solid solution.

Precipitates are formed in various morphologies like needles, ribbons, disks and spheres [14-17]. The most often reported intermetallic is  $\text{Ni}_3\text{Mo}$ . In the initial stages of aging the  $\text{Ni}_3\text{Mo}$  metastable precipitation is favoured because of the low lattice misfit between the precipitate and the matrix. Aging for longer times and/or higher temperature ( $>480^\circ\text{C}$ ) leads to a gradual increase in coherency stresses and the  $\text{Ni}_3\text{Mo}$  is therefore replaced by a more stable Mo-containing precipitate such as  $\text{Fe}_2\text{Mo}$  or  $\sigma$ -phase (Fe-Mo) [1].

The titanium-containing intermetallic most often found to precipitate during aging is  $\mu\text{-Ni}_3\text{Ti}$  but the presence of the  $\sigma$  ( $\text{FeTi}$ ) phase has also been reported occasionally. It is possible that some more complex intermetallics such as  $\text{Ni}_3(\text{MoTi})$  are also formed in the process of aging.

The mechanisms of different precipitation processes are not fully understood. There is some evidence that pre-precipitate zones may form during the initial stages of age hardening. Garwood and Jones [17] have suggested that there is a G.P. zone stage in which segregates are formed parallel to the  $[111]_{\text{bcc}}$  direction. In Ti containing alloys, Miller and Mitchell [14] suggested that titanium initially forms metastable, ordered bcc zones of  $\text{Ni}_3\text{Ti}$ . These zones are subsequently replaced by  $\eta\text{-Ni}_3\text{Ti}$ .

The nucleation of the precipitates during aging generally occurs on dislocations and lath boundaries. Because of

the high density and uniformity of dislocations in the lath martensite, the precipitates are homogeneously distributed unless a preferred orientation of dislocation exists. In case of preferred orientation of dislocations, precipitates may also get oriented [14, 17].

Takaki and Tokunaga [18] have investigated the aging reaction using specific heat, hardness and resistivity measurements. Figure 1.6 shows the specific heat versus temperature curves of ternary and quarternary martensitic alloys. A heat evolution occurring around  $347^{\circ}\text{C}$  ( $620^{\circ}\text{K}$ ) corresponds to formation of an ordered phase. The ordered phase [19] is suggested to be  $\text{Fe}(\text{Ni},\text{Co})$ . The  $467^{\circ}\text{C}$  ( $740^{\circ}\text{K}$ ) peak evolution is due to the formation of Mo rich zones [20-23] and the absorption around  $497^{\circ}\text{C}$  ( $770^{\circ}\text{K}$ ) is due to the reversion of these zones.

It has been shown that the critical condition [23] for appearance of  $467^{\circ}\text{C}$  ( $740^{\circ}\text{K}$ ) evolution peak is given by the following expression

$$\% \text{Co} \times \% \text{Mo} = 32 \quad (1.1)$$

The  $527^{\circ}\text{C}$  ( $800^{\circ}\text{K}$ ) peak evolution is attributed to formation of  $\text{Ni}_3\text{Mo}$  [15].

Takaki and Tokunaga [18] concluded that age hardening of Ni maraging steels without Ti or Al addition is mainly due to the formation of Mo rich zones prior to the precipitation of  $\text{Ni}_3\text{Mo}$ .

#### 1.4.1. CONVENTIONAL HEAT TREATMENT OF MARAGING STEEL

As mentioned earlier, microstructures of heat-treated maraging steels consist of fine precipitates of intermetallic compounds uniformly distributed in a matrix of Fe-Ni martensite [1]. Such a microstructure is conventionally achieved by a

two-stage heat treatment involving

(a) solution treatment in the austenitic phase field followed by martensitic transformation.

(b) Aging of martensite

The commercial heat treatment of these steels consists of solutionising at  $820^{\circ}\text{C}$  for 1 hr per 25 mm section thickness followed by air cooling and then ageing at  $480^{\circ}\text{C}$  for 3 hrs [3].

#### 1.4.2. UNCONVENTIONAL HEAT TREATMENTS OF MARAGING STEELS

The basic microstructural unit controlling the strength and fracture of lath martensites has been suggested to be the packet [24-30] or block [31,32]. Because blocks in 18% Ni maraging steels consist of a set of parallel laths with essentially the same variant and are separated from one another by high angle boundaries [5] it should be considered that the block in maraging steel is the basic structural unit of lath martensite structure to act as a barrier to deformation and fracture.

Maki et al have studied the relationship between prior austenite grain size and packet size and block width [6]. Variation of packet size and block width and the ratio of grain size to packet size (G.S./P.S.) with prior austenite grain size has been shown in Figures 1.7 and 1.8 respectively. It can be seen that both packet size and block width as well as G.S./P.S. decrease by decreasing the prior austenite grain size.

It is not surprising, therefore, that efforts are made to develop alternative heat treatments for maraging steels from the point of view of refinement of prior austenite grains. Specifically,  $\alpha' \rightarrow \gamma$  cyclic transformation and several thermomechanical treatments such as cold rolling before solution

treatment and hot rolling during cooling from the solution temperature [33] have been attempted. Further, since the nature of the precipitation of intermetallic compounds and their aging kinetics are likely to be affected by the distribution of alloying elements within the martensitic structure, the effect of solution treatment temperature and cooling rates have also been subjected to re-examination. For example, Muneki et al. have observed that by solutionizing at conventional temperature, i.e.  $820^{\circ}\text{C}$ , a part of Mo remains as the retained precipitate, which reduces the ductility and toughness leading to the easy occurrence of unstable fracture at a low stress level [34]. It was suggested, therefore, to perform the solutionizing at higher temperature. A new heat treatment schedule [2] has been suggested according to which the solutionising is carried out in two stages. It consists of annealing at  $930 \pm 10^{\circ}\text{C}$  for 80 minutes, air cooling and re-annealing at  $760 \pm 10^{\circ}\text{C}$  for 80 minutes followed by air cooling. It is then aged at  $480^{\circ}\text{C}$  for 3 hrs. Some investigators [2] have reported a better combination of strength and toughness, if a double annealing treatment is employed prior to ageing. However, metallurgical reasons for the enhancement of properties by the double annealing treatment have not been clearly given.

#### 1.5 DYNAMIC STRAIN AGING OF 18 Ni MARAGING STEELS :

It has been generally accepted that the hardening of Ni maraging steels at the conventional aging temperature (conventional aging temperature is  $480^{\circ}\text{C}$ ) is due to the precipitation of the intermetallic compound involving Mo on dislocations introduced by the martensitic transformation [18]. However, it is probable that the nature of aging kinetics is

complex prior to the precipitation of the intermetallic compound [18]. For example, Peters and Cupp [20] have suggested that at aging temperatures below 457°C, Mo rich zones, [20-23] named "matrix precipitates", are formed in the matrix away from dislocations. But Takaki and Tokunaga [18] suggested that Mo rich zones are formed within the stress field of dislocations by "a kind of strain aging".

Hayes [35] examined the aging kinetics of the 18 Ni 250 maraging steel under dynamic aging conditions. Hayes [35] studied the dynamic aging of 18 Ni 250 maraging steel by conducting a series of uniaxial tensile test on single solutionized samples. The test temperatures were varied from 204 to 454°C and the strain rate from  $1.16 \times 10^{-4}$  to  $1.5 \times 10^{-2} \text{ s}^{-1}$ .

### 1.5.1 Phenomenology

In a tensile [36] test, the specimen (suitably gripped between two cross heads, one moving and the other fixed) is deformed at a constant nominal strain rate determined by the velocity of the moving cross head. At any instant of time, the total strain  $\epsilon$ , the plastic strain  $\epsilon_p$  in the specimen, and the elastic strain  $\epsilon_e$  of the specimen machine system are related by

$$\epsilon = \epsilon_p + \epsilon_e \quad (1.2)$$

$$\dot{\epsilon} = \dot{\epsilon}_p + \dot{\epsilon}_e \quad (1.3)$$

$$= \dot{\epsilon}_p + \frac{\dot{\sigma}}{E_s} \quad (1.4)$$

where  $\dot{\sigma}$  is the stress rate,  $E_s$  is the elastic modulus of the specimen-machine system,  $\dot{\epsilon}$  is the imposed strain rate and  $\dot{\epsilon}_p$  is the plastic strain rate.

The condition for load drop/serrations is that the plastic

strain rate  $\dot{\epsilon}_p$  exceeds the imposed strain rate  $\dot{\epsilon}$ , i.e., whenever there is a sudden increase in  $\dot{\epsilon}_p$  a load drop occurs.

### 1.5.2 Physical processes that cause serrated flow :

(i) *Ordering* : In alloys undergoing order-disorder [36] transformation, gradients or modulations in order encountered by moving dislocations can lead to serrated flow. In case of short range order stress will increase by an amount,  $\Delta\sigma$  given by [37]

$$\Delta\sigma = \gamma/b \quad (1.5)$$

where  $\gamma$  is the increase in the surface energy of slip plane, since a dislocation of burgers vector  $b$  in its passage will lower the order of the lattices. If in an avalanche of dislocations this order is destroyed rapidly, a drop in flow stress will result.

This theory was later extended by Schoeck and Seeger [38]. The basic concept of "Schoeck ordering" is that if an ordered arrangement of atoms causes distortion in the lattice, the formation of an ordered region around dislocations will be favoured in those positions where the lattice strain due to ordering complies with the local stress tensor of the dislocation i.e. where elastic strain energy in the crystal is reduced by ordering. In other words, the line energy of the dislocation is lesser by a certain amount compared with a dislocation surrounded by a random or disordered distribution of solutes. In order to move the dislocation we have to apply a certain force since we must supply energy to bring the dislocation into a region where there is random distribution of solutes. Since for the process of ordering, only atomic interchanges between neighbouring lattice sites are necessary and no long range diffusion of atoms is involved, it takes place in a relatively short time and is not

influenced by the concentration of vacancies in the material.

Low value of activation energy in CuAu [39] has been attributed to enhanced migration of atoms in a narrow region (a few burgers vector wide) near the core of the dislocation.

(ii) *Twinning* : Another phenomenon that can cause serrations is continued mechanical twinning as has been reported for an Fe-25 at% Be alloy [36].

(iii) A sudden increase in the specimen temperature due to adiabatic heating is another possibility. This has been found to occur in tests at cryogenic temperatures [36].

(iv) Phase transformations induced by stress and strain can also cause serrated flow [36].

**CHAPTER 2****Aim of the present work :**

The purpose of the present study is to examine the dynamic strain aging behaviour of 18 Ni 250 maraging steel for novel heat treatment conditions as discussed in Chapter 1. It is intended to shed more light on the physical processes associated with dynamic strain aging. Also it is intended to study the effect of a novel heat treatment on the microstructural features of 18 Ni 250 maraging steel.

## CHAPTER III

### EXPERIMENTAL PROCEDURES

#### 3.1 MATERIAL

Commercial grade of maraging 250 steel in the form of sheets was obtained from Mishra Dhatu Nigam Ltd, Hyderabad. The material was manufactured by double vacuum melting followed by ingot making, rough forging, hot rolling and cold rolling. The supplied material was in two batches; the sheet thickness of material of batch 1 being 2.2 mm and that of batch 2 being 4.8 mm.

The chemical composition of the material supplied is shown in Table 3.1.

#### 3.2 THERMOMECHANICAL TREATMENT

Samples of approximately 65 mm x 40 mm x 4.8 mm were cut from the sheets of Batch 2. These samples were homogenized at  $1014^{\circ}\text{C}$  for 60 minutes in a horizontal muffle furnace. The homogenizing furnace, made of Inconel tube, had the capability of providing controlled atmosphere. Homogenizing treatment of all the samples was done under argon atmosphere.

Homogenized and preheated samples were subsequently hot rolled on a 2-high rolling mill having 135 mm diameter rolls rotating at a speed of 55 rpm. A total of 82% thickness reduction was given in 9 passes. Details of the thermomechanical working schedule are shown in Table 3.2. A schematic diagram of the rolling schedule is shown in Figure 3.1. All the hot rolled sheets were immediately water quenched (within 5 s) after the final pass.

### 3.3 HEAT TREATMENT

As mentioned earlier, sheet samples of maraging 250 steel were obtained in two batches. Samples from the second batch were subjected to thermomechanical treatment discussed in Section 3.2. Tensile test samples from both materials, non-thermomechanically treated (Batch 1) and thermomechanically treated (Batch 2), were made. Tensile test samples as well as samples for microstructural examinations were subjected to single and double solution treatments. Samples were subject to single solution treatment in a muffle furnace made of Inconel tube and sealed from one end. The furnace had a constant temperature zone of ~ 70 mm in length and had a provision of heat treating under argon atmosphere. Both single and double solution treatments were carried out under argon atmosphere. The following conditions were followed for heat treatments .

#### A. Single Solution Treatment :

Holding of samples at a temperature of  $935^{\circ}\text{C}$  for 35 minutes followed by quenching in agitated water.

#### B. Double Solution Treatment :

(i) Holding of samples at a temperature of  $935^{\circ}\text{C}$  for 35 minutes followed by quenching in agitated water.

(ii) Holding of samples at a temperature of  $760^{\circ}\text{C}$  for 45 minutes followed by quenching in agitated water.

### 3.4 DYNAMIC STRAIN AGING TESTS

#### 3.4.1 The Tensile Test

A series of uniaxial tensile tests were conducted over a

range of strain rates and at several temperatures.

Tensile specimens were machined and polished on lathe centres. Figure 3.3 shows the standard dimensions of the tensile test specimen. The test pieces were flat.

Testing was performed on an Instron testing machine. All test temperatures were monitored on a multipoint strip chart recorder with a type K thermocouple attached directly to the gauge length of the specimen. The test temperatures,  $T$  were varied from  $286^{\circ}\text{C}$  to  $400^{\circ}\text{C}$  and the strain rates were varied from  $7.95 \times 10^{-5}$  to  $9.55 \times 10^{-3} \text{ s}^{-1}$ . Details of the tensile test are shown in Table 3.3. All testing was performed in air. All load-strain curves were recorded to rupture.

### 3.4.2 Measurement of Stress Decrement vs Strain Rate

From the load elongation plot shown schematically in Figure 3.4 the average height of the serration is determined. The stress decrement,  $\sigma_D$  is calculated by using the following equation [40]

$$\sigma_D = \frac{P}{A_0} (e+1) \quad (3.1)$$

where  $P$  is the height of the serration,  $A_0$  is the original area of cross section of the specimen and  $e$  is the engineering strain. The average true strain rate,  $\dot{\epsilon}$  is given by [40]

$$\dot{\epsilon} = \left[ \frac{v}{l_0} + \frac{v}{l_f} \right] \frac{1}{2} \quad (3.2)$$

where  $v$  is the cross head velocity,  $l_0$  is the initial gage length

and  $l_f$  is the final gage length of specimen after fracture.

### 3.4.3 Calculation of Activation Energy

At each temperature the stress decrement,  $\sigma_D$ , is plotted as a function of  $\log \dot{\epsilon}$  as shown schematically in Figure 3.5. At any particular value of stress decrement,  $\sigma_D$ , a straight line (shown as dotted line in Figure 3.5) is drawn parallel to  $\log \dot{\epsilon}$  axis. The values of  $\log \dot{\epsilon}$ , found from Figure 3.5, are plotted as a function of reciprocal of temperature as shown in Figure 3.6.

The activation energy,  $\Delta H$ , is calculated by using the following equation proposed by Hayes [41-43] [See appendix-1 for derivation].

$$-\Delta H = \left[ \frac{R \log \dot{\epsilon}}{\frac{1}{T} \log e} \right] \sigma_D \quad (3.3)$$

Let the slope of the graph shown in Figure 3.6 be  $m_1$ . Hence  $\Delta H$  is determined by the following equation

$$m_1 = \frac{-\Delta H \log e}{R \times 10^3} \quad (3.4)$$

### 3.5 MICROSCOPY

In order to study the structural changes associated with thermomechanically treated and single and double solution treated samples, specimens were prepared for their microstructural examination by optical microscopy, scanning electron microscopy (SEM) and transmission electron microscopy (TEM). Experimental procedures adopted for these purposes are described below.

### 3.5.1 Optical Microscopy

Metallography samples from as-received, thermomechanically treated and heat treated samples were mechanically polished by standard methods to achieve optimum polished surface. The 18% Ni 250 maraging steel is known to exhibit a typical lath martensite. However, the etching is generally difficult to clearly reveal the martensitic structure, especially the packet boundaries [6]. Etching the lath martensite structure of steels used in the present study, therefore, required considerable amount of experimentation. Etching reagents which were tried have been shown in Table 3.4. but results obtained were not found to be satisfactory.

To detect the prior austenite grain boundaries, the specimens were aged at  $520^{\circ}\text{C}$  for 25 mts and electrolytically etched in a 10% chromic acid ( $\text{Cr}_2\text{O}_3$ ) solution. The experimental set up is shown in Figure 3.2. The polished specimen, S, serves as the anode and C is the steel cathode. The temperature of the electrolyte was maintained at room temperature and voltage was maintained at 6 volts. The etched specimens were seen in optical microscope.

### 3.5.2 Scanning Electron Microscopy

Metallography samples from as-received, thermomechanically treated and heat treated samples were mechanically polished by standard methods to achieve optimum polished surface. The specimens were etched chemically or electrolytically. The etched specimens were seen in the scanning electron microscope at 15 KV.

### 3.5.3 Transmission Electron Microscopy

Specimens were mechanically thinned down to about 80 microns. Then discs of 3 mm diameter were punched out. The discs were electrojet polished using perchloric acid and acetic acid in the ratio of 1:9. The temperature of the electrolyte was maintained at 7°C and voltage was maintained as 25 volts.

After jet polishing the specimens were observed in the transmission electron microscope at 80 KV and/or 100 KV.

## CHAPTER 4

## RESULTS AND DISCUSSION

4.1 Dynamic strain aging behaviour of maraging steels :

4.1.1 Dynamic strain aging behaviour of double solutionized samples without subjecting them to TMT.

(i) During the tensile test the serrations/stress drops were accompanied by an audible acoustic emission.

(ii) The typical dynamic strain aging behaviour curve is shown in Figure 4.01. It must be noted that serrated yielding starts at a particular value of strain and continues right up to the fracture of the specimen. In other words there was only one stage of serrated yielding. In all the double solutionized samples of batch 1, fracture preceded the disappearance of the serrated yielding.

(iii) Stress decrement ( $\sigma_D$ ) as a function of strain rate ( $\dot{\epsilon}$ ) at a given temperature :

In Figure 4.02 it can be seen that stress decrement ( $\sigma_D$ ) decreases as the strain rate ( $\dot{\epsilon}$ ) increases at constant temperature.

Mathematically the plastic strain rate ( $\dot{\epsilon}_p$ ) [44] is expressed as

$$\dot{\epsilon}_p = \rho_m b v \quad (4.1)$$

where  $\rho_m$  is the mobile dislocation density,  $b$  is the burgers vector and  $v$  is the dislocation velocity. The dislocation velocity,  $v$  is given by [44]

$$v = \frac{\ell}{t_w + t_f} \quad (4.2)$$

where  $\ell$  is the distance between obstacles,  $t_w$  is the waiting time

of dislocation at an obstacle and  $t_f$  is the flight time of the dislocation. Since  $t_w \gg t_f$  equation 4.2 reduces to the form

$$v = \frac{\ell}{t_w} = \frac{1}{(\rho_f)^{1/2} t_w} \quad (4.3)$$

where  $\rho_f$  is the forest dislocation density. Hence equation [44] 4.1 can be rewritten as

$$\dot{\epsilon}_p = \frac{b \rho_m (\rho_f)^{-1/2}}{t_w} \quad (4.4)$$

From equation 4.4, it can be seen that as the plastic strain rate  $(\dot{\epsilon}_p)$  increases, the waiting time  $(t_w)$  decreases.

In terms of waiting time  $(t_w)$ , Figure 4.02 implies that the stress decrement  $(\sigma_D)$  increases as the waiting time  $(t_w)$  increases. This is in agreement with the models proposed for dynamic strain aging. In these models [45] the solute concentration as "seen" by the dislocation increases with increase in waiting time  $(t_w)$ . Also Hayes [35] has suggested that increase in stress decrement  $(\sigma_D)$  represents an increase in atmosphere size. To put it simply, anchoring force of dislocation atmosphere is represented by  $\sigma_D$ . This anchoring force increases with increase in waiting/arrest time  $(t_w)$  of dislocation held up at a barrier.

(iv) Stress decrement  $(\sigma_D)$  as a function of temperature at constant strain rate :

In Figure 4.02 it can be seen that the stress decrement  $(\sigma_D)$  increases with increase in temperature at a given strain rate.

It has been suggested by Hayes [35] that increase in stress

decrement ( $\sigma_D$ ) represents an increase in atmosphere size with increasing temperature at constant strain rate.

But it is well known from thermodynamic principles that the atmosphere binding energy decreases as temperature increases. The decrease in atmosphere binding energy with increase in temperature is considered in the Fermi-Dirac model proposed by Barnett et al [46]. It is shown in this treatment that the binding energy is decreasing due to increasing thermal fluctuation of dislocations which are enhanced by the increasing temperature. From this point of view, it has been explained that decrease in atmosphere binding energy with increasing temperature results in atmospheres becoming progressively weaker as the temperature increases. However, as the temperature increases, the diffusion rate of the atmosphere species also increases thus allowing atmosphere growth to occur. This has been treated by Cottrell [47]. Hayes [42] has proposed that increase in atmosphere size may more than offset the decrease in binding energy which occurs with temperature increase in temperature/regions in which the Portevin-le chatelier effect is observed.

The Fermi-Dirac atmosphere model proposed by Barnett et al [46] also shows that solute atmospheres do not evaporate as the temperature increases. The present study on 18-Ni maraging steel tends to support the Fermi-Dirac atmosphere model proposed by Barnett et al.

It is probable that the energy barrier which a dislocation must overcome before escaping [42] from an atmosphere is dominated by the increasing atmosphere size rather than the decreasing binding energy in temperature/strain rate ( $\dot{\epsilon}$ ) ranges where the

Portevin le chatelier effect/serrated yielding is observed.

(v) Flow stress ( $\sigma$ ) at 2% strain as a function of temperature and strain rate :

In Figure 4.03 it can be seen that at any temperature there is a decrease in flow stress ( $\sigma$ ) as the strain rate ( $\dot{\epsilon}$ ) increases. In other words, a negative strain rate sensitivity exists.

This can be understood in terms of equation 4.4 discussed in Section 4.1.1. From the equation 4.4 it is clear that as the plastic strain rate increases, waiting time ( $t_w$ ) decreases. Hence flow stress decreases as strain rate ( $\dot{\epsilon}$ ) increases at a given temperature.

Also at constant strain rate there is an increase in flow stress with increase in temperature. It has been suggested [35] that this is due to gradual increase in atmosphere size.

(vi) Activation energy :

From Figure 4.02 and figure 4.04 the activation energy,  $\Delta H$ , is calculated by using the stress decrement ( $\sigma_0$ ) method discussed in Section 3.4.3.

The activation energy was found to be 1.2445 eV. It is interesting to note that the value of activation energy,  $\Delta H$  obtained by Peters and Cupp [20] based on hardness measurements is in excellent agreement with the value obtained in the present study. Hayes [35] has also obtained similar activation energy values and has suggested that the values of  $\Delta H$  for the low temperature ( $< 316^{\circ}\text{C}$ ) static precipitation process (matrix clustering) and low-temperature dynamic precipitation process (atmosphere formation) are similar.

(vii) Critical strain ( $\epsilon_c$ ) as a function of strain rate and

temperature :

From Figure 4.05 which shows double logarithmic plots of critical strain versus strain rate, we see that these plots exhibit a thermally activated or "normal" increasing branch [44] and a descending branch of inverse strain rate dependence separated by a "minimum". This behaviour is pronounced at 286°C and 350°C. At 400°C we see a minima and the "normal" increasing branch. This anomalous dependence might be connected with precipitation before and during the deformation test [44].

The mechanism by which critical strain is affected is not understood [44]. In fact, this anomalous dependence reinforces the case for using stress decrement ( $\sigma_D$ ) method for understanding dynamic strain aging. The efficacy of the stress decrement ( $\sigma_D$ ) method vis-a-vis the critical strain ( $\epsilon_c$ ) approach has been discussed by Hayes [41-43] [see appendix 2 for details].

4.1.2 Dynamic strain aging behaviour of samples that have been subjected to thermomechanical treatment followed by double solutionizing :

- (i) During the tensile test the serrations were accompanied by an audible acoustic emission.
- (ii) The typical dynamic strain aging behaviour curve is shown in Figure 4.06. The curve shows two stages or domains of serrated yielding. Figure 4.07 is a schematic plot defining the critical strains.

It has been suggested [44] that onset of serrated yielding occurs when the (strain dependent) strain rate sensitivity turns negative. In other words critical strains are defined from the condition of vanishing of the strain rate sensitivity. Actually

the critical strain,  $\epsilon_c$  is sometimes found to be larger than the strain at which strain rate sensitivity vanishes [48]. It has been suggested that [48] critical condition of vanishing of the strain rate sensitivity may be met several times (upto four times) along a deformation curve.

(iii) Critical strains as a function of strain rate and temperature :

From Figure 4.08, which shows double logarithmic plots of critical strain ( $\epsilon_{c_1}$ ) versus strain rate ( $\dot{\epsilon}$ ) at different temperatures, we see a "normal" increasing branch [44] at  $286^{\circ}\text{C}$  and  $400^{\circ}\text{C}$ . But at  $350^{\circ}\text{C}$  the behaviour seems irregular.

(iv) First Critical Strain :

From Figure 4.05 and Figure 4.08 it must be noted that the first critical strain ( $\epsilon_{c_1}$ ) is lower than in double solutionized samples of batch 1 which have not been subjected to thermomechanical treatment. This might be partly due to higher mobile dislocation density in thermomechanically treated samples.

(v) Number of stages/domains as a function of strain rate at constant temperature :

From Table 4.18, Table 4.17, Figure 4.06 and Figure 4.09 we see that number of stages/domains of jerky flow/serrated yielding decreases as the strain rate ( $\dot{\epsilon}$ ) increases at a given temperature. This trend in which two different domains of serrated flow expand towards each other with increasing strain rate ( $\dot{\epsilon}$ ) and merge at a well defined strain value has been reported for a Cu - 3.3 at % Sn alloy by Räuchle et al [49].

But at  $286^{\circ}\text{C}$  this trend seems to be violated as shown in Table 4.16.

(vi) Stress decrement ( $\sigma_D$ ) during dynamic strain aging as a function of temperature and strain rate :

In Figure 4.1 it can be seen that the stress decrement follows the same trends as described for double solutionized samples of batch 1 in section 4.1.1.

Moreover for a given strain rate ( $\dot{\epsilon}$ ) and temperature (T) stress decrement ( $\sigma_D$ ) increases as we go from lower domains to higher domains of serrated yielding. This trend is shown in Table 4.12, 4.13, 4.14, 4.16, 4.17 and 4.18. Hence in general at a given strain rate and temperature, atmosphere size increases as we go from low strain regimes to high strain regimes.

(vii) Activation Energy :

From Figure 4.1 and Figure 4.11 the activation energy,  $\Delta H$  for the final stage of serration is calculated by using the stress decrement ( $\sigma_D$ ) method discussed in Section 3.4.3. The activation energy,  $\Delta H$  was found to be 1.2633 eV.

This implies that the final stage involves similar mechanism for both double solutionized samples and samples subjected to thermomechanical treatment followed by double solutionizing. Also since stress decrement ( $\sigma_D$ ) is lower for the initial domains of serrated flow as shown in Figure 4.06 and tables 4.12, 4.13, 4.14, 4.16, 4.17, 4.18, the activation energy values will be lower for the initial stages. Hence it is suggested that initial domains/stages of serrated flow require lower activation energy.

#### 4.1.3 Models for dynamic strain aging

Hayes [35] has proposed a model to explain the dynamic strain aging behaviour of 18 Ni 250 maraging steels. The proposed model for dynamic aging of 18 Ni maraging steel is summarized as follows

[35] :

(i) at temperatures below  $316^{\circ}\text{C}$ , the predominant hardening mechanism is the interaction of Mo atoms with the dislocations to form atmospheres. As the aging temperature increases, the solute atmospheres continue to grow. Simultaneously, Mo-rich clusters may be nucleating in the matrix away from the dislocations or pre-exist in the matrix.

(ii) above  $316^{\circ}\text{C}$ , the Mo atoms diffuse down the dislocation lines (pipe diffusion) to the clusters. The rate-controlling step for the delay and the subsequent aging process is suggested to be the rate of Ni diffusion through the Fe matrix to the Mo clusters so that  $\text{Ni}_3\text{Mo}$  can be formed. This reaction rate increases with increasing temperature and/or decreasing strain rate.

(iii) as the aging process progresses further, the reaction at the bcc Mo clusters begins to saturate. The dislocations then begin to retain their Mo atmospheres. At this point, aging continues by a direct reaction between the Ni atoms and the remaining Mo atmospheres on the dislocation line. The rate-controlling process for this reaction is the bulk diffusion of the Ni to the dislocation lines to form the  $\text{Ni}_3\text{Mo}$  precipitates directly on the dislocations.

Hayes [35] model satisfactorily explains the manifestations of dynamic strain aging behaviour. But according to the specific heat curves (see Fig. 1.6) obtained by Takaki and Tokunaga [18] Mo atmospheres form within the stress field of dislocations at around  $467^{\circ}\text{C}$ . Moreover the serrations in the present investigation were accompanied by an audible acoustic emission. Hence it is suggested that the serrations might be due to twinning. Twinning

can lead to serrations as has been reported for an Fe-25 at% Be alloy [36].

Another possible cause of serrations can be formation of an ordered phase like Fe (Ni, Co). The specific heat curves obtained by Takaki and Tokunaga [18] shows a heat evolution around  $347^{\circ}\text{C}$  which is likely due to an ordering reaction. A.F. Yednreal et al. [19] have obtained an evidence for ordering in an aged Fe-16% Ni-26%Co martensitic alloy by electron microscopic analysis and suggested that the ordered phase may be Fe(Ni, Co).

#### **4.2 Microstructure of 18 Ni 250 maraging steel**

##### **4.2.1 Microstructures of batch 1 specimens :**

Grain size memory effect can be seen from the optical and scanning electron micrographs. There is no appreciable difference in grain size between as received (ARB1) [Figure 4.12], as received + single solutionized (ARB1 + SS) [Figure 4.15] and as received + double solutionized (ARB1 + DS) [Figure 4.17] as shown in Table 4.19.

The chemically etched structures of as received (ARB1) [Figure 4.14], as received + single solutionized (ARB1 + SS) [Figure 4.16] and as received + double solutionized (ARB1 + DS) [Figure 4.19 and Figure 4.20] are characterised by well developed packets.

The electrolytically etched structures of as received (ARB1) [Figure 4.12], as received + single solutionized (ARB1 + SS) [Figure 4.15] and as received + double solutionized (ARB1 + DS) [Figure 4.17] are characterized by well developed prior austenite grain boundaries. The scanning electron micrograph of as received specimen (ARB1) [Figure 4.13] shows the packets inside a prior

austenite grain.

The transmission electron micrograph of as received specimen (ARB1) [Figure 4.21] shows the lath structure.

#### **4.2.2 Microstructures of batch 2 specimens :**

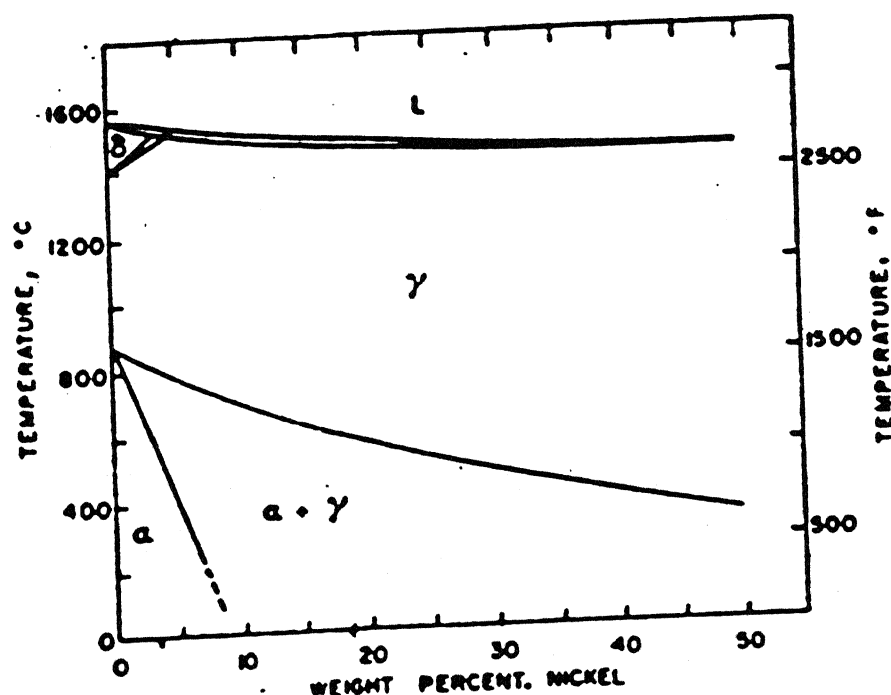
Grain size memory effect can be seen from the optical and scanning micrographs. There is no appreciable difference in grain size between as received + single solutionized (ARB2 + SS) [Figure 4.24], as received + double solutionized (ARB2 + DS) [Figure 4.26], as received + thermomechanically treated (ARB2 + TMT) [Figure 4.29], as received + thermomechanically treated + single solutionized (ARB2 + TMT + SS) [Figure 4.37] and as received + thermomechanically treated + double solutionized (ARB2 + TMT + DS) [Figure 4.40] as shown in Table 4.19.

The chemically etched structures of as received (ARB2) [Figure 4.23], as received + single solutionized (ARB2 + SS) [Figure 4.25], as received + double solutionized (ARB2 + DS) [Figure 4.27], as received + thermomechanically treated (ARB2 + TMT) [Figure 4.34, 4.35 and 4.36], as received + thermomechanically treated + single solutionized (ARB2 + TMT + SS) [Figure 4.38 and Figure 4.39] show well developed packets. It must be noted that the as received + thermomechanically treated + double solutionized (ARB2 + TMT + DS) [Figure 4.41 and Figure 4.42] are not optically resolved and do not show well developed packets.

On comparing the optical micrograph of as received (ARB2) [Figure 4.22] and as received + thermomechanically treated (ARB2 + TMT) [Figure 4.29] it must be noted that no appreciable grain refinement has taken place due to thermomechanical treatment. But

on comparing the transmission electron micrograph of as received (ARB1) [Figure 4.21] with as received + thermomechanically treated (ARB2 + TMT) [Figure 4.43], it must be noted that the lath width has refined by thermomechanical treatment. Also the transmission electron micrograph of as received + thermomechanically treated + double solutionized (ARB2 + TMT + DS) [Figure 4.44] shows finer laths compared to as received + thermomechanically treated (ARB2 + TMT) [Figure 4.43].

On comparing the as received + double solutionized (ARB2 + DS) [Figure 4.27] with as received + thermomechanically treated + double solutionized (ARB2 + TMT + DS) [Figure 4.41] it must be noted that while (ARB2 + DS) [Figure 4.27] is resolved in the optical micrograph, (ARB2 + TMT + DS) [Figure 4.41] is not resolved. Also from the scanning electron micrograph of (ARB2 + TMT + DS) [Figure 4.45] it can be seen that the blocks have become very fine. Also the transmission electron micrographs of ARB2 + TMT + DS [Figure 4.44] shows very fine laths.



[Courtesy Iron Steel Inst.  
FIG1.1 Iron-rich portion of the iron-nickel equilibrium diagram.  
(Owen and Liu.)

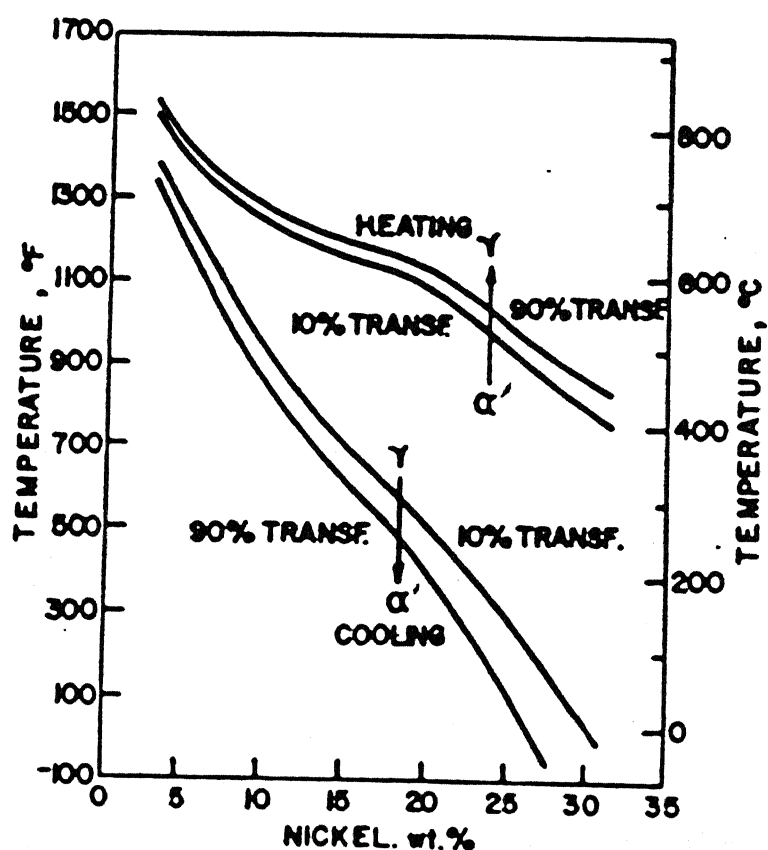


FIG.1.2 Metastable Iron-Nickel Phase Diagram.

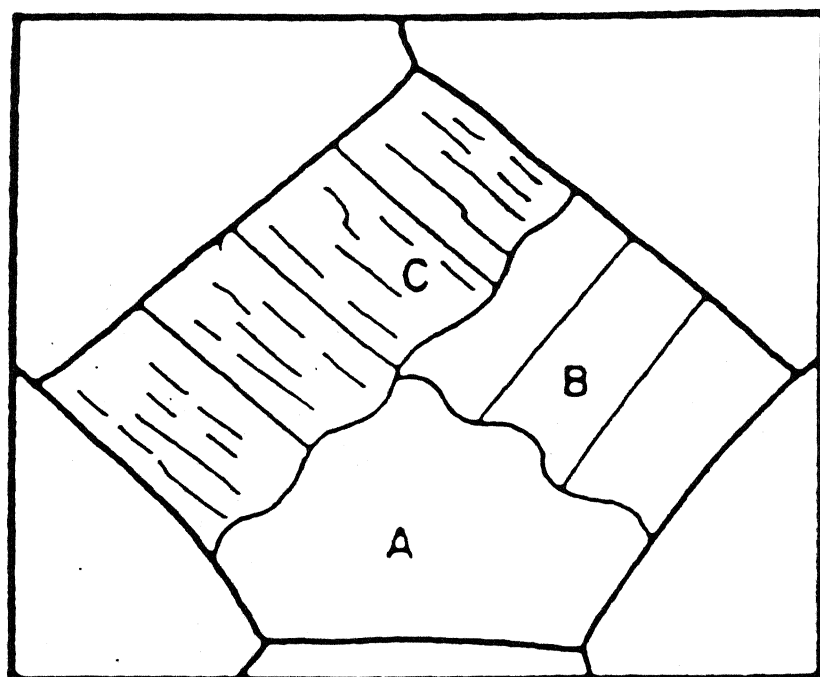


FIG 1.3 Schematic illustration showing the construction of lath martensite structure in a prior austenite grain reported by J. M. Marder and A. R. Marder.<sup>11</sup> Section A represents a packet, section B shows blocks within a packet and section C illustrates an aligned substructure within the block of a packet.

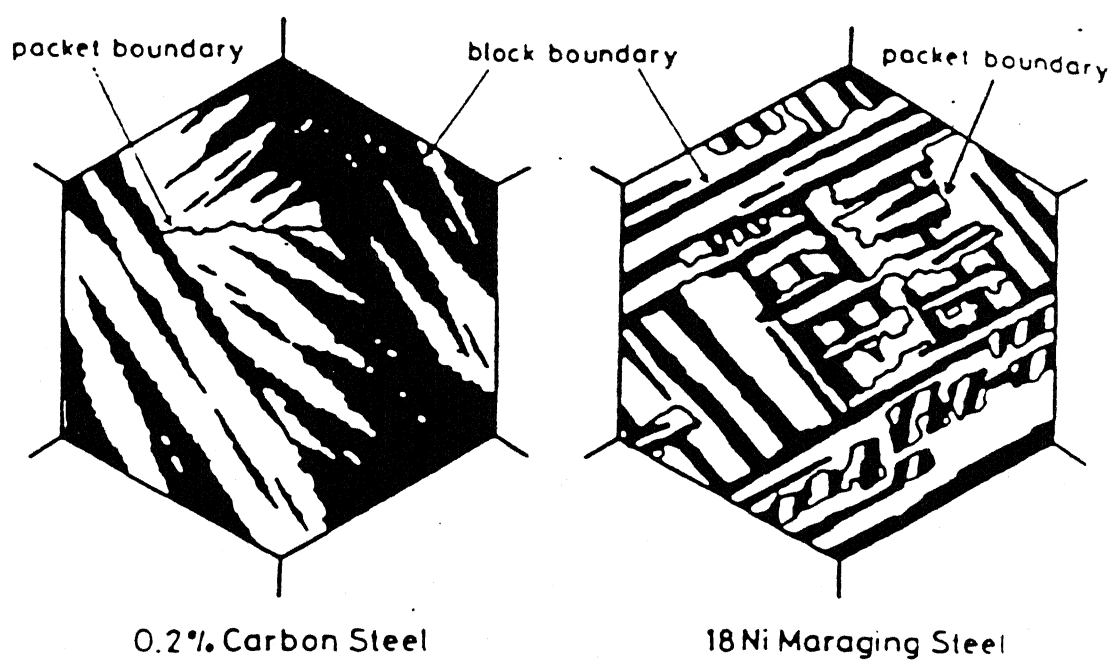


FIG.1-4 Schematic illustrations showing the morphological characteristics of lath martensite structure in 0.2% C steel and 18% Ni maraging steel.

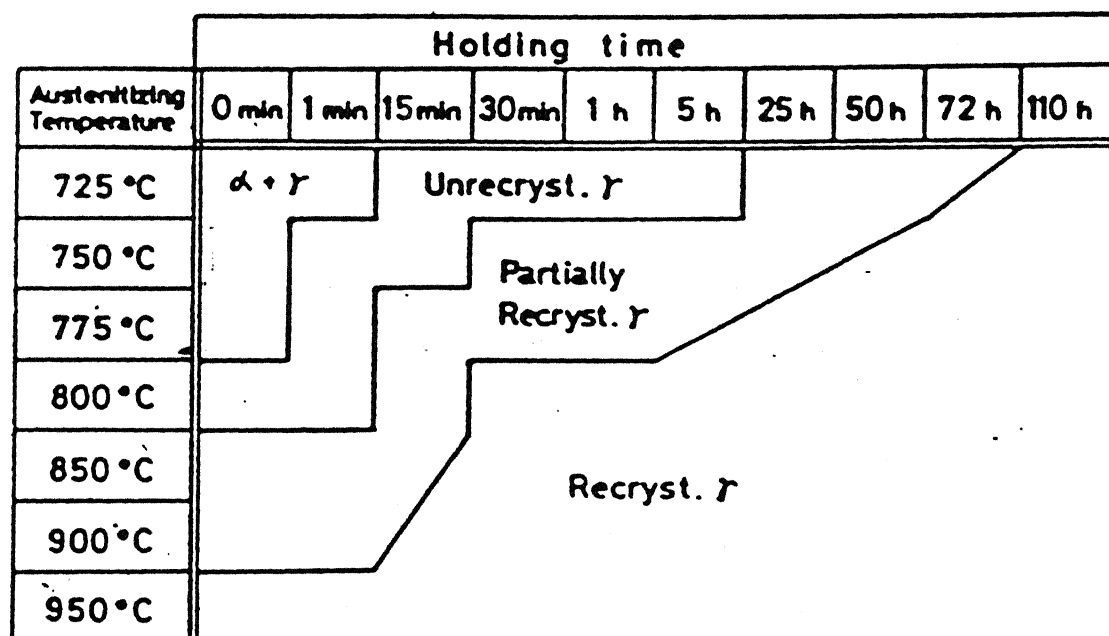


FIG.1.5 Structure change of reversed austenite with holding (austenitizing) temperature and holding time in 18%Ni maraging steel (heating rate: 100°C/min); solution treated specimen.

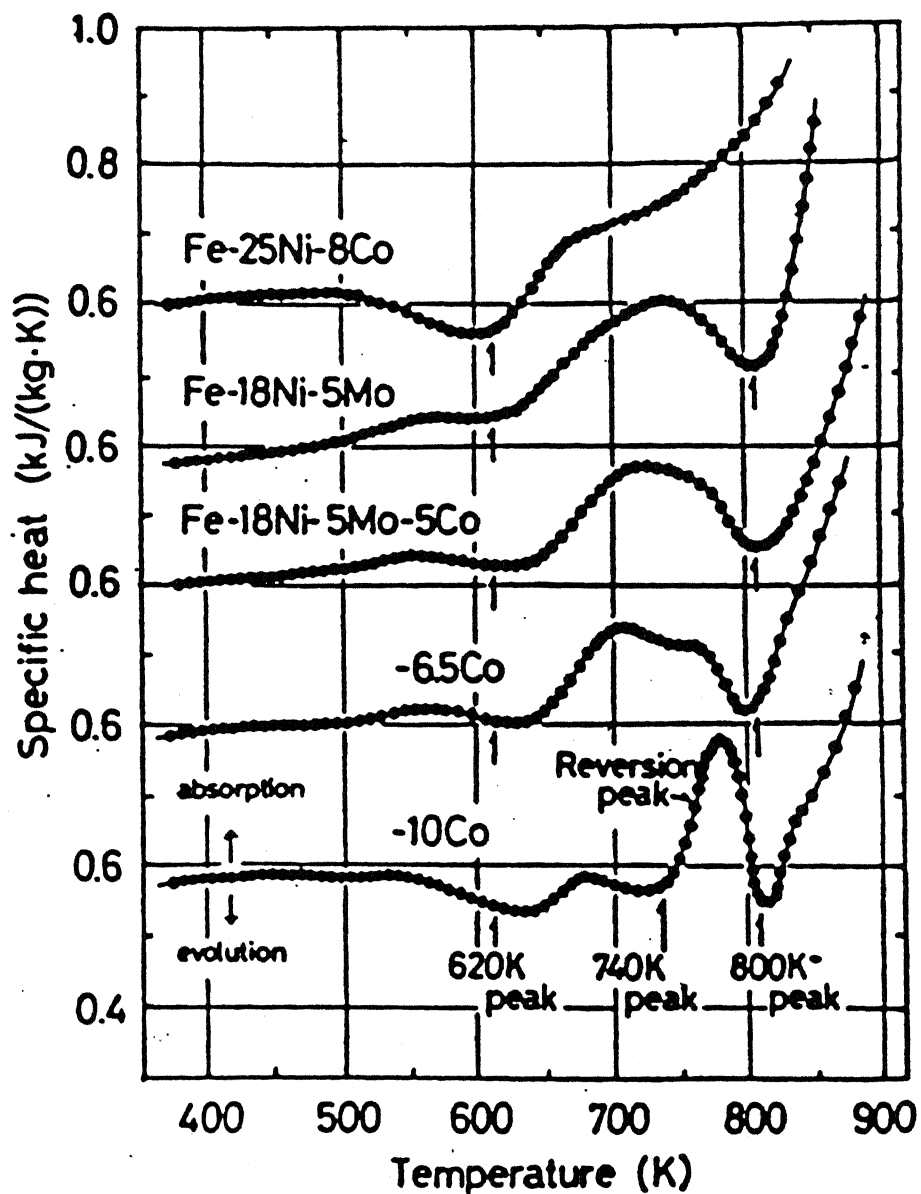


FIG.1.6 Specific heat versus temperature curves of the ternary and quaternary alloys: Heating rate is about 0.025 K/s.

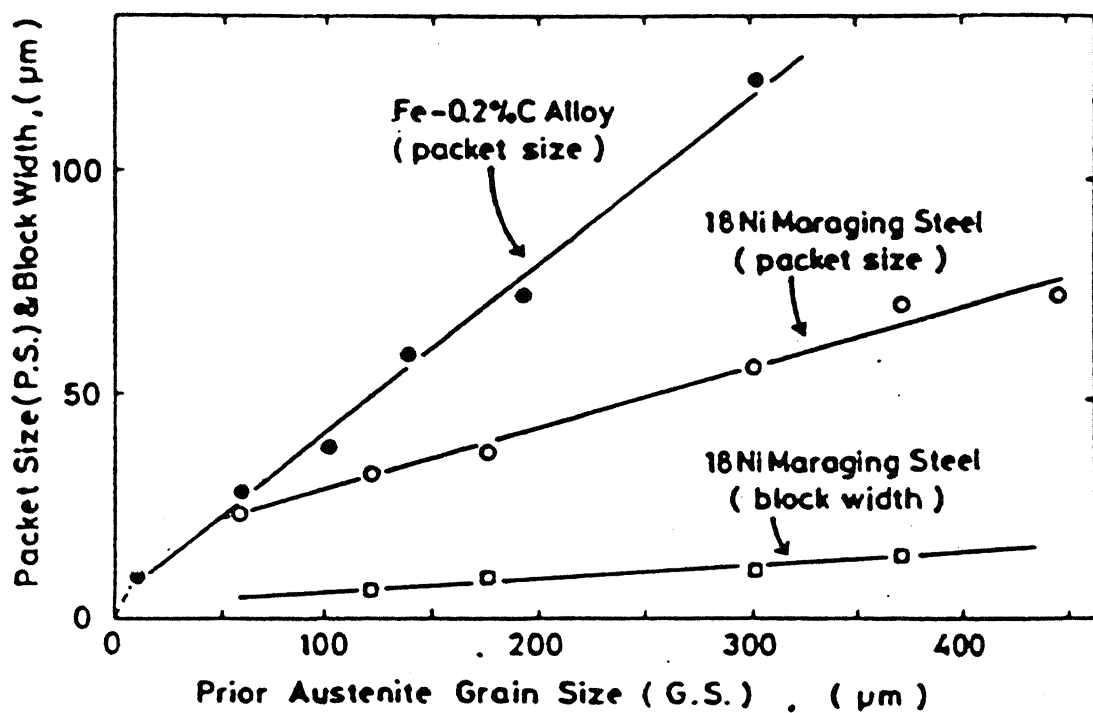


FIG.1.7 Change in the packet size and block width of lath martensite with the prior austenite grain size in Fe-0.2%C alloy and 18%Ni maraging steel.

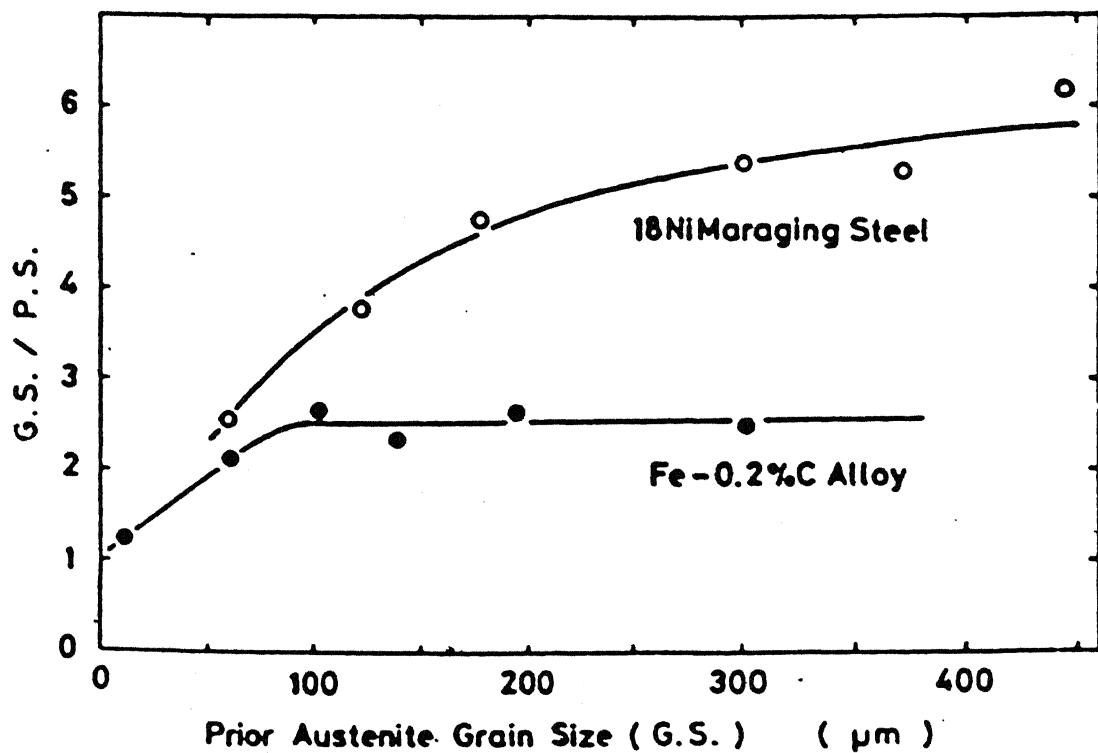


FIG.1.8 Change in the ratio of G.S. (prior austenite grain size) to P.S. (packet size of lath martensite) with the prior austenite grain size in Fe-0.2%C alloy and 18%Ni maraging steel.

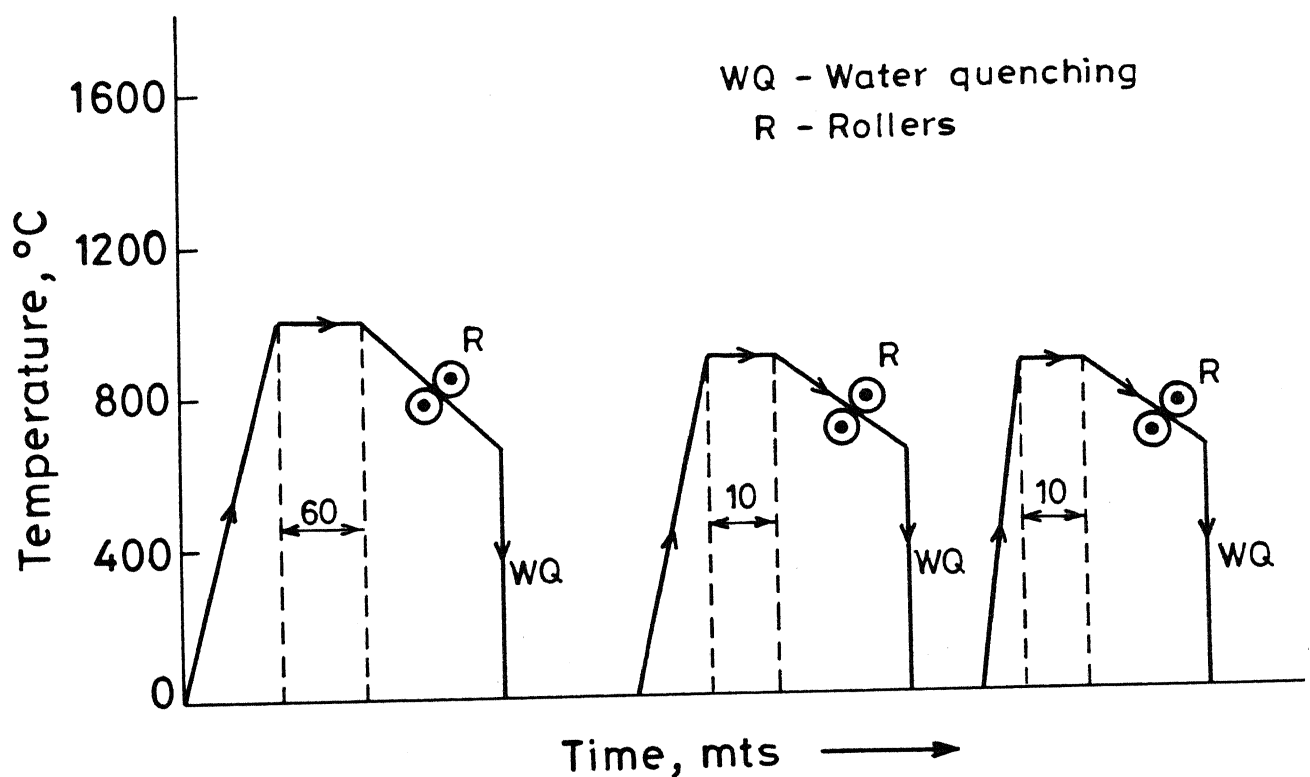


Fig. 3.1 Temperature - time diagram showing thermomechanical treatment.

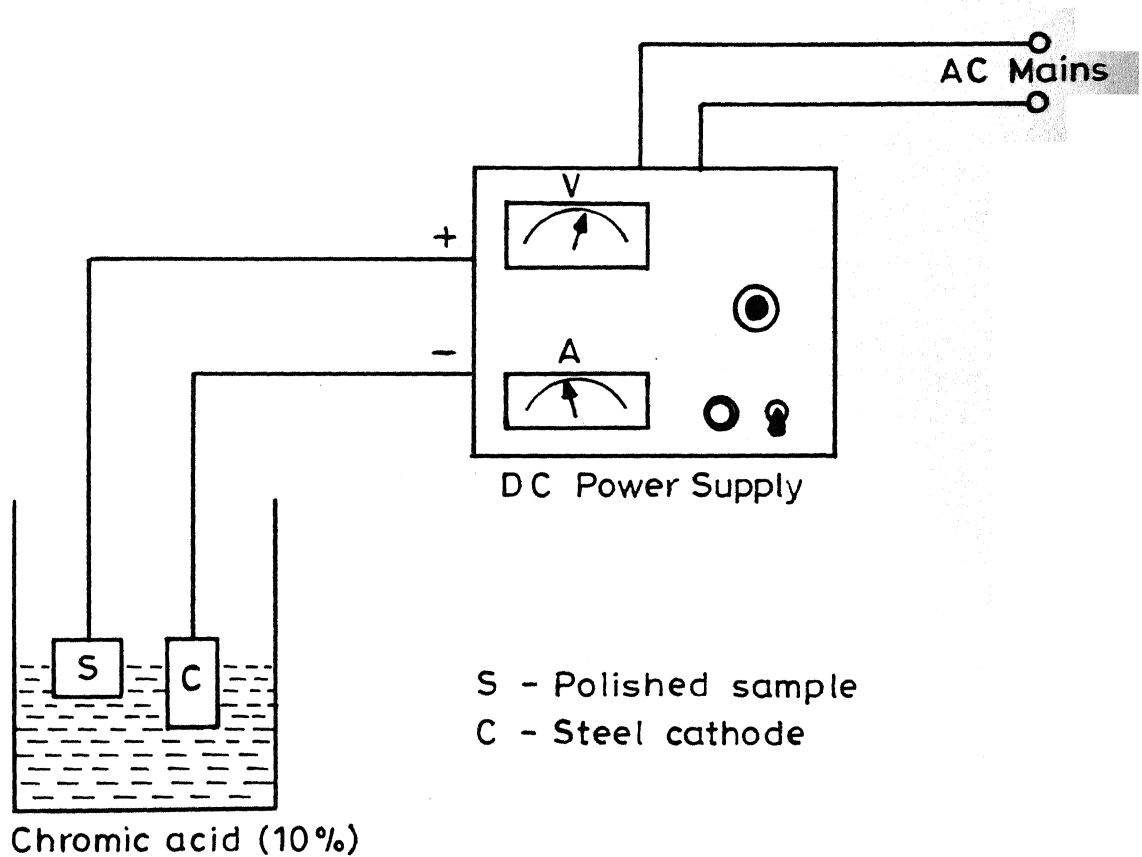


Fig. 3.2 Electrolytic etching apparatus.

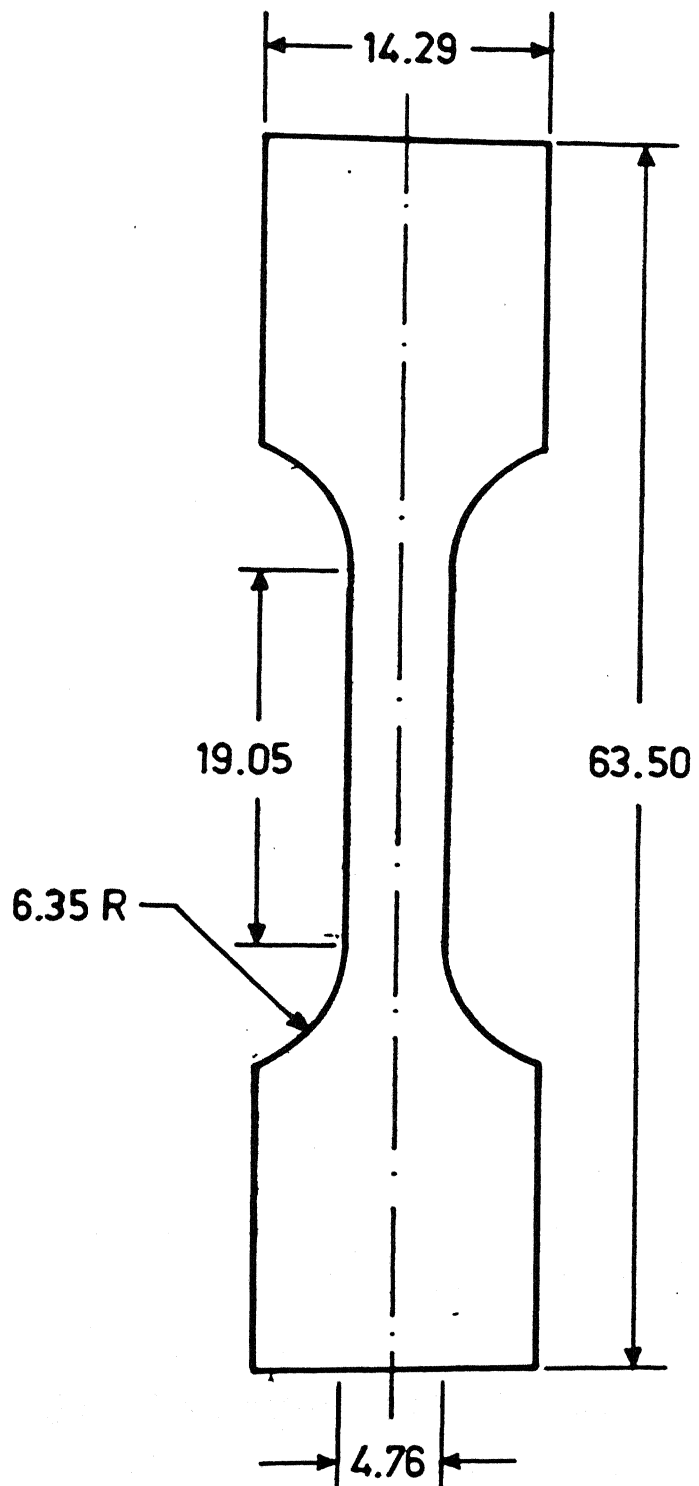


Fig.3.3 Tensile test specimen (units in mm)

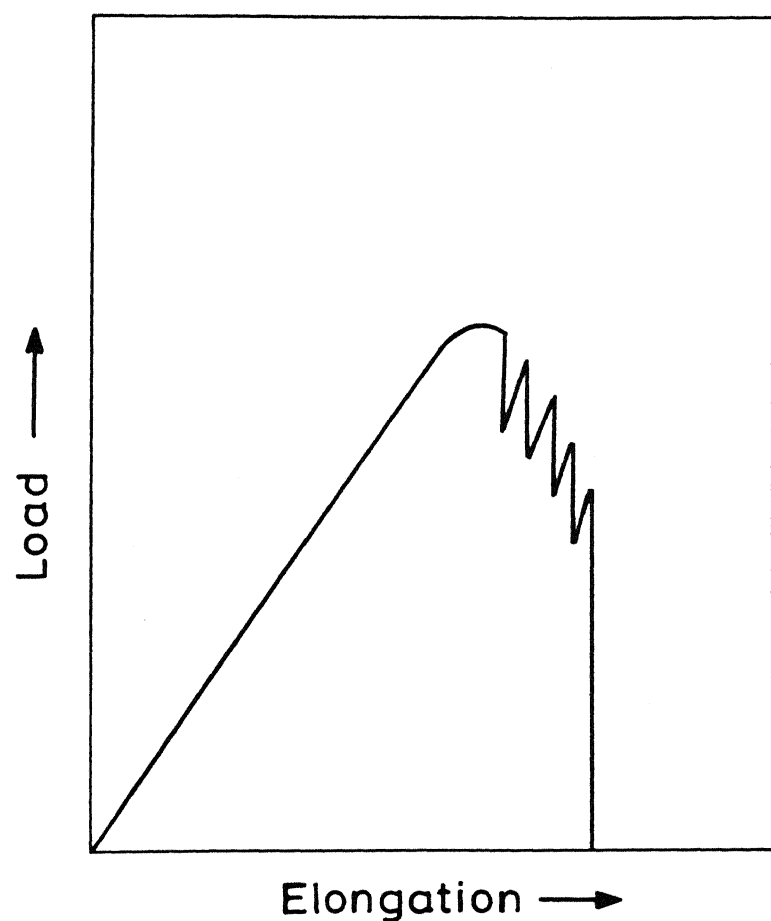


Fig. 3.4 Schematic plot of load vs elongation.

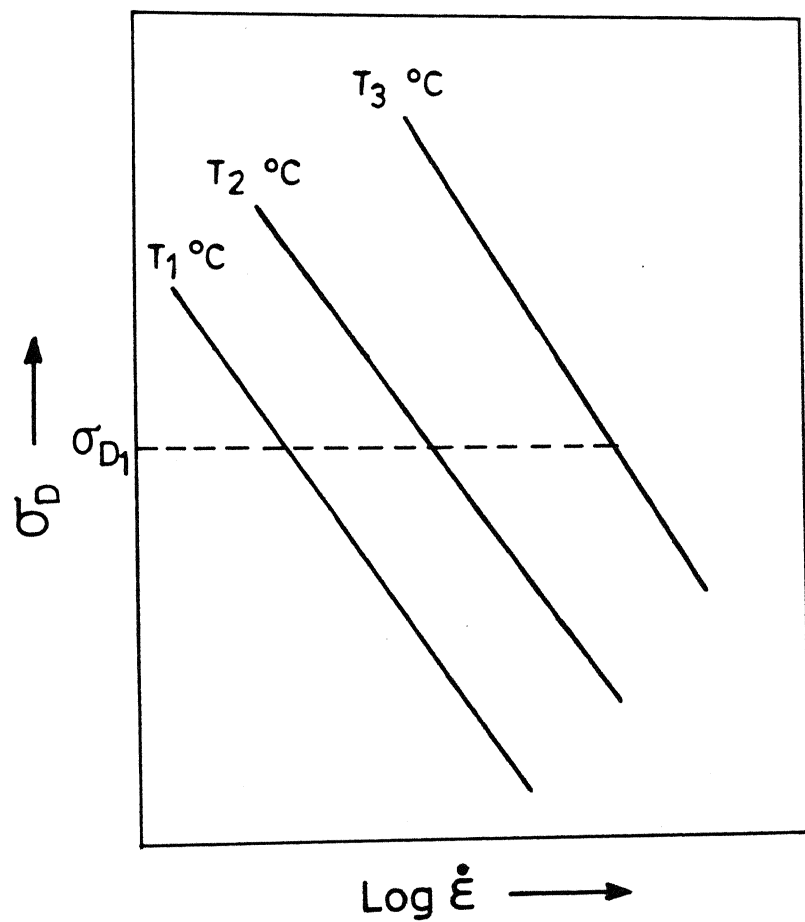


Fig. 3.5 Schematic plot of stress decrement,  $\sigma_D$ , as a function strain rate,  $\dot{\epsilon}$ , at different temperatures.

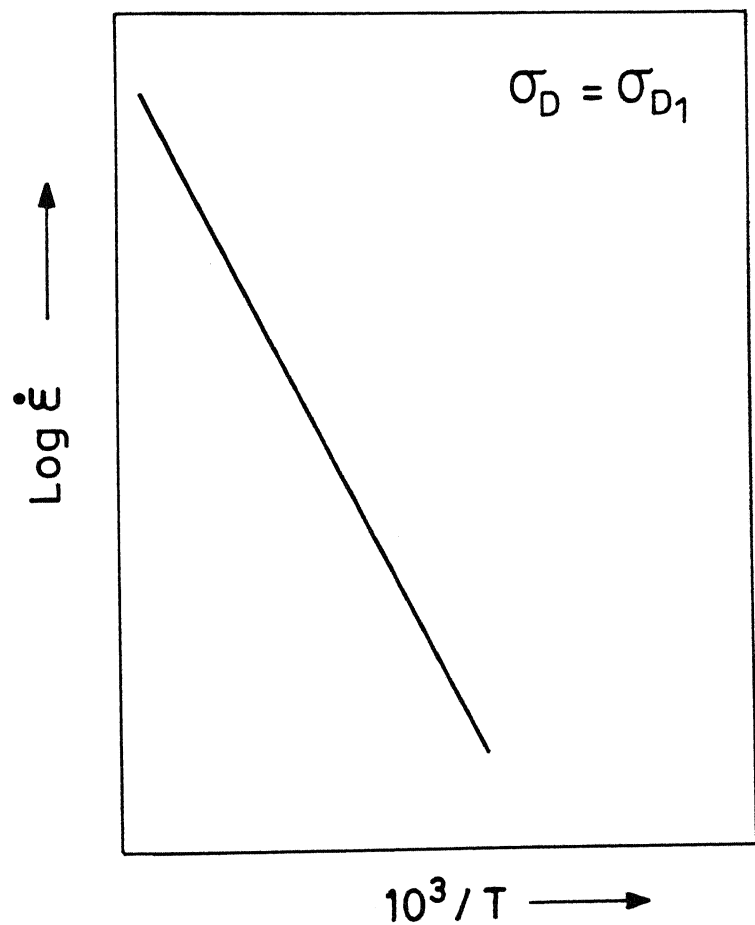


Fig.3.6 Schematic plot of  $\log \dot{\epsilon}$  as a function reciprocal of temperature at constant stress decrement,  $\sigma_{D1}$ .

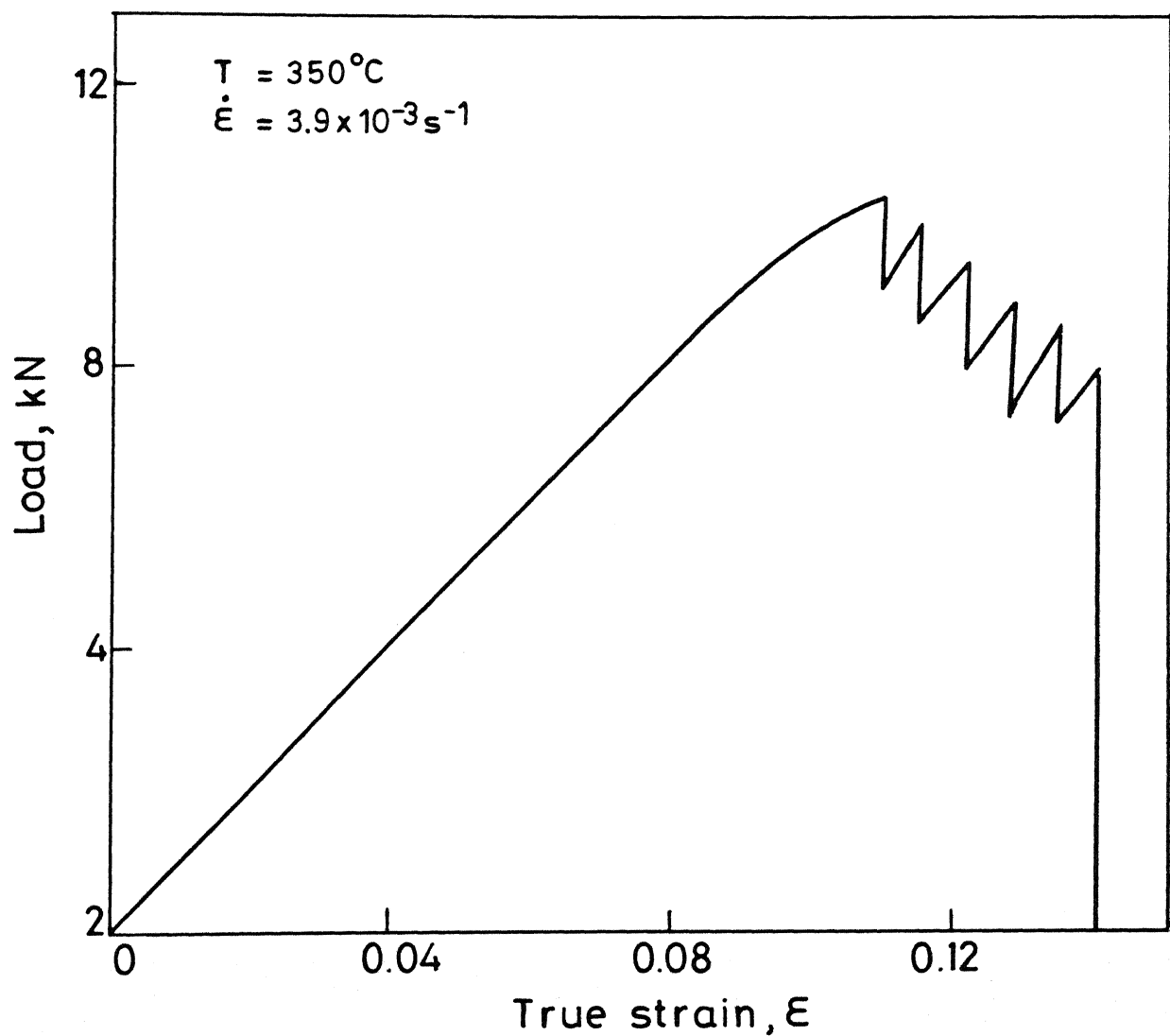


Fig.4.01 Variation of load with elongation (ARB1+ DS).

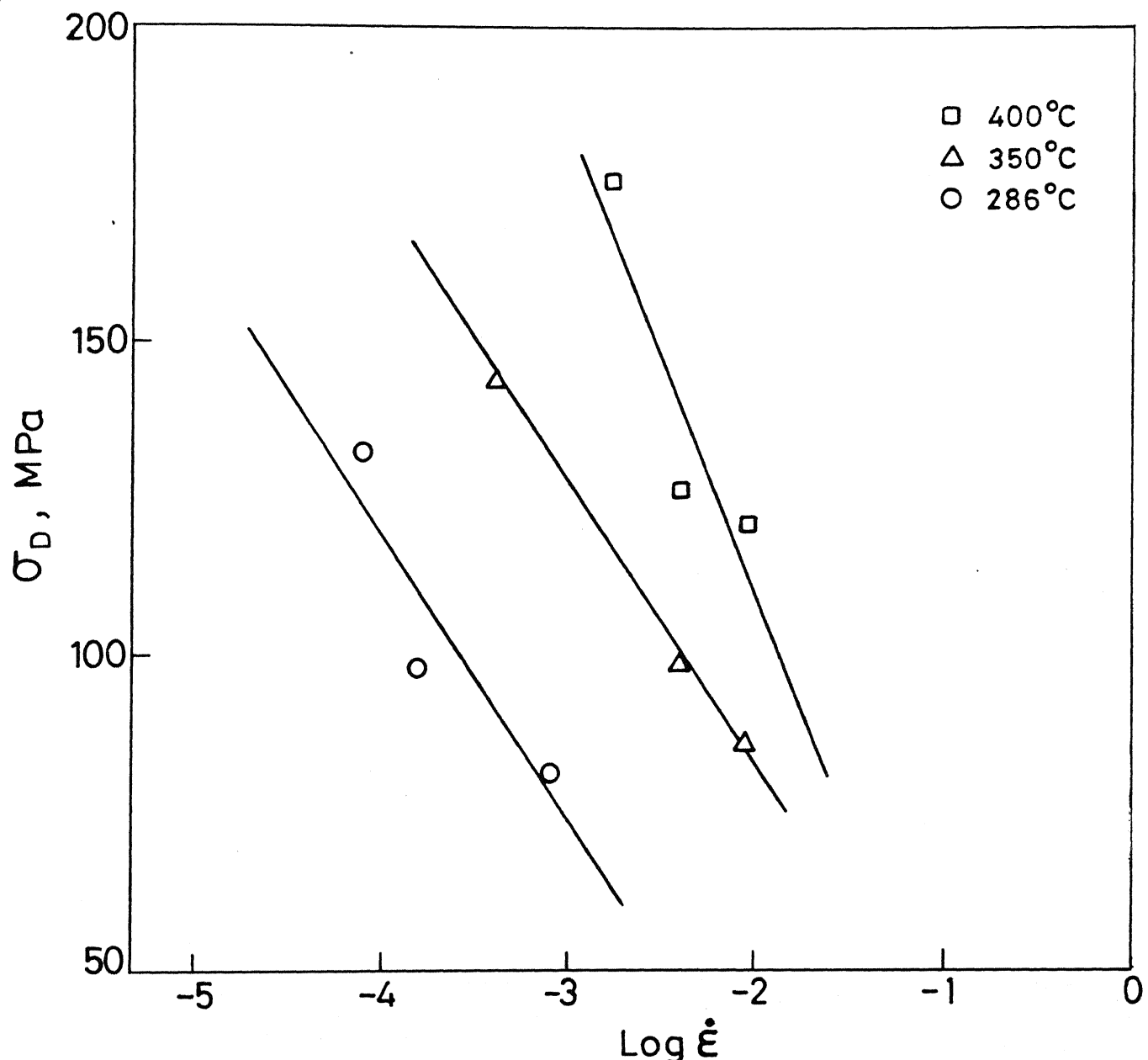


Fig. 4.02 Variation of stress decrement  $\sigma_D$  at 8.3% strain as a function of strain rate,  $\dot{\epsilon}$  at different temperatures (ARB1+DS)

CENTRAL LIBRARY  
I.I.T., KANPUR

Acc. No. A112498

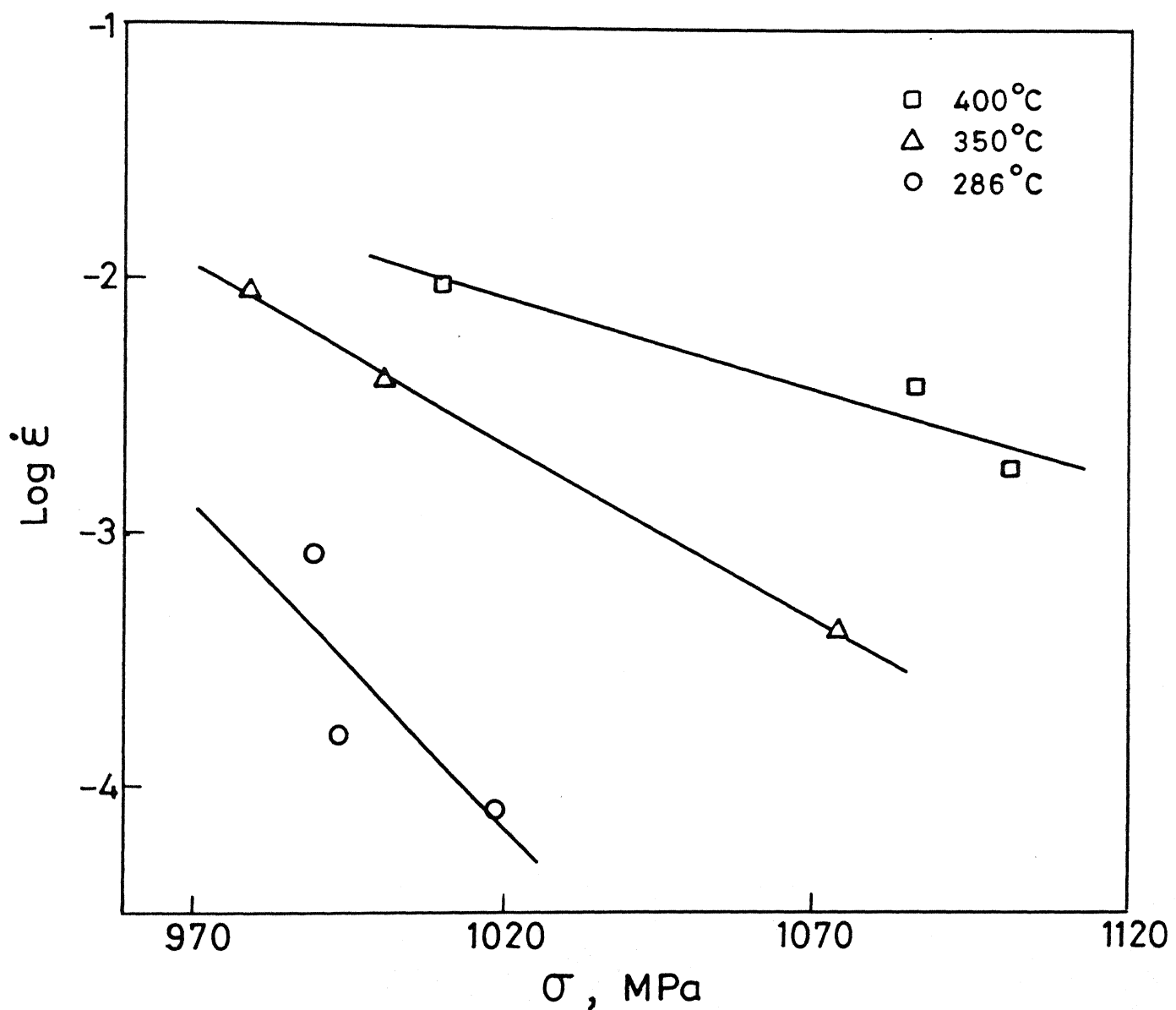


Fig. 4.03 Variation of flow stress,  $\sigma$  at 2% strain as a function of strain rate,  $\dot{\epsilon}$  at different temperatures (ARB1+DS)

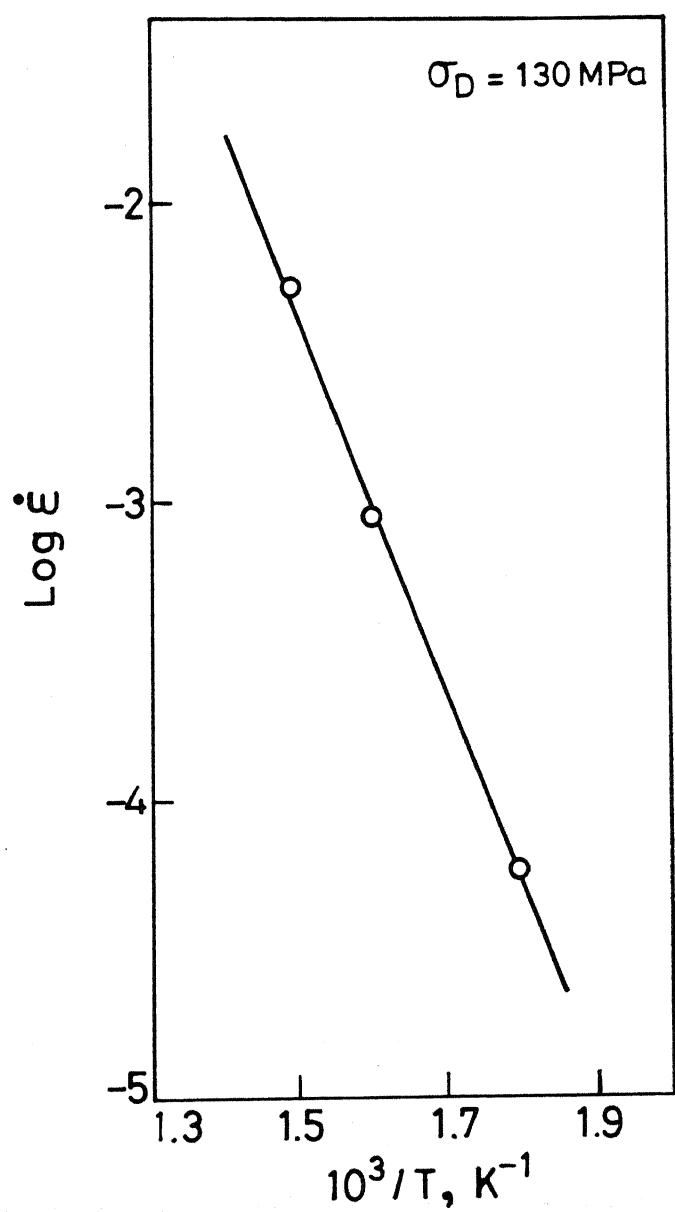


Fig. 4.04 Variation of strain rate,  $\dot{\epsilon}$  as a function of temperature at constant stress decrement,  $\sigma_D$  (ARB1 + DS)

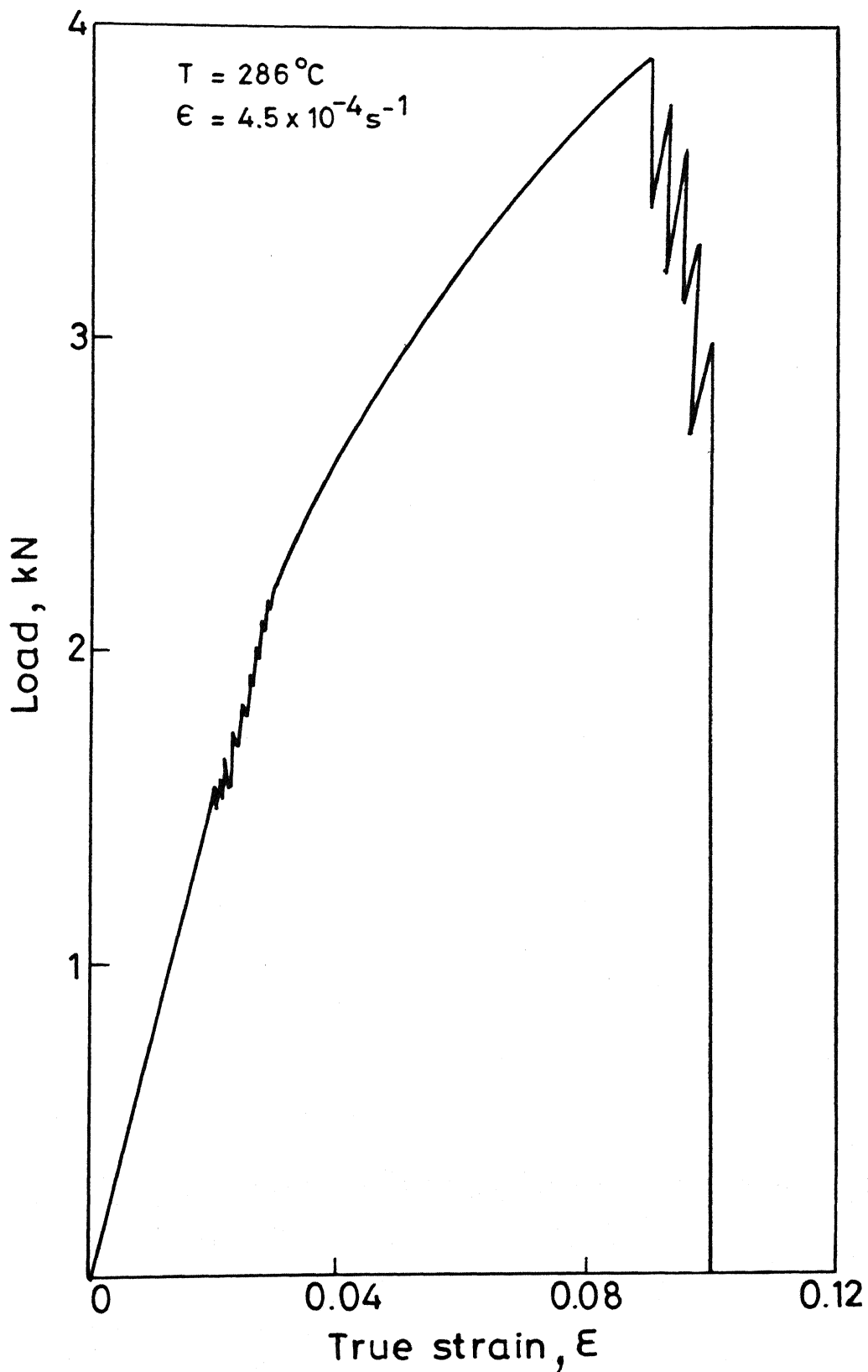


Fig. 4.06 Variation of load with elongation (TMT + DS).

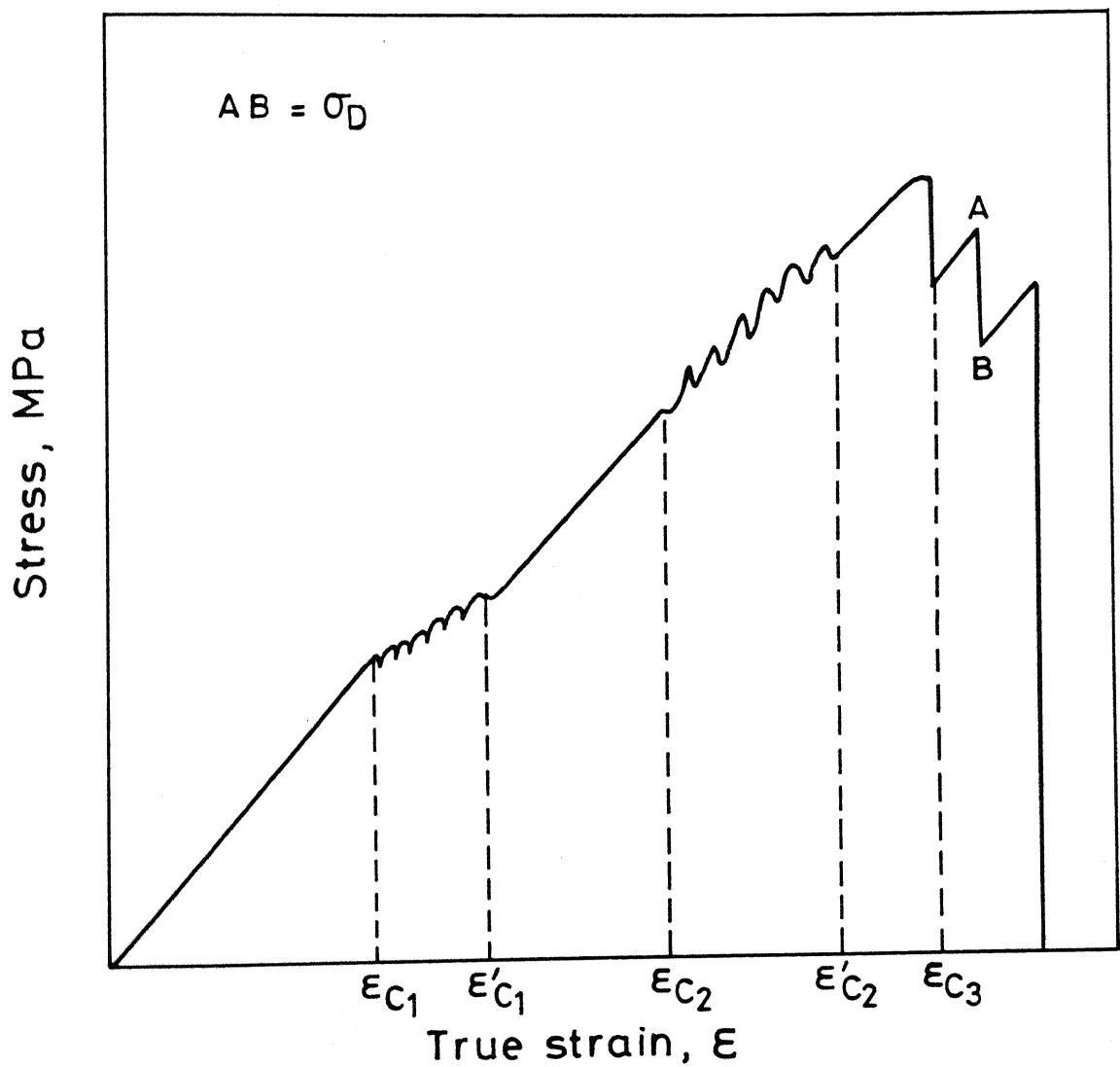


Fig.4.07 Variation of stress with elongation  
(TMT/TMT+SS/TMT+DS).

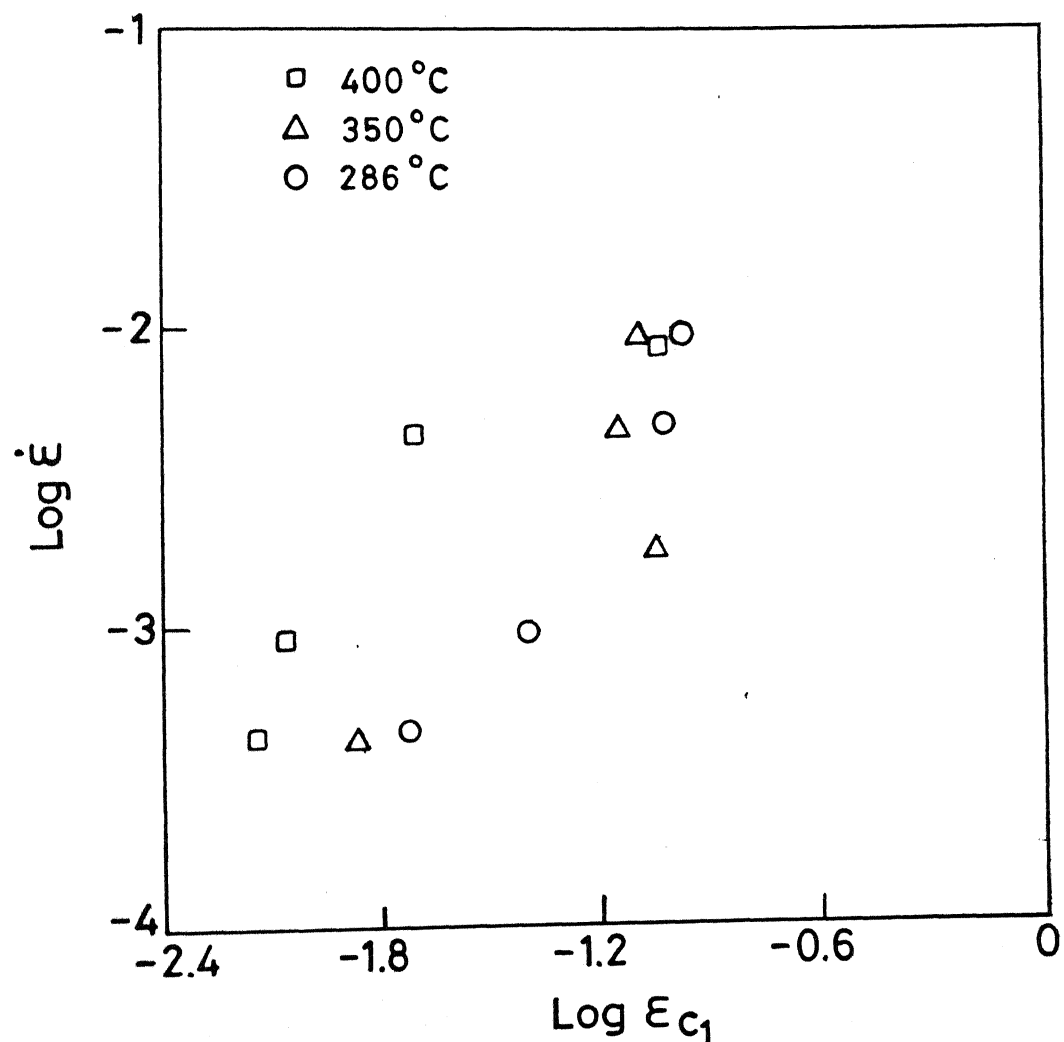


Fig. 4.08 Variation of first critical strain,  $E_{c1}$  as a function of strain rate,  $\dot{\epsilon}$  at different temperatures (TMT+DS)

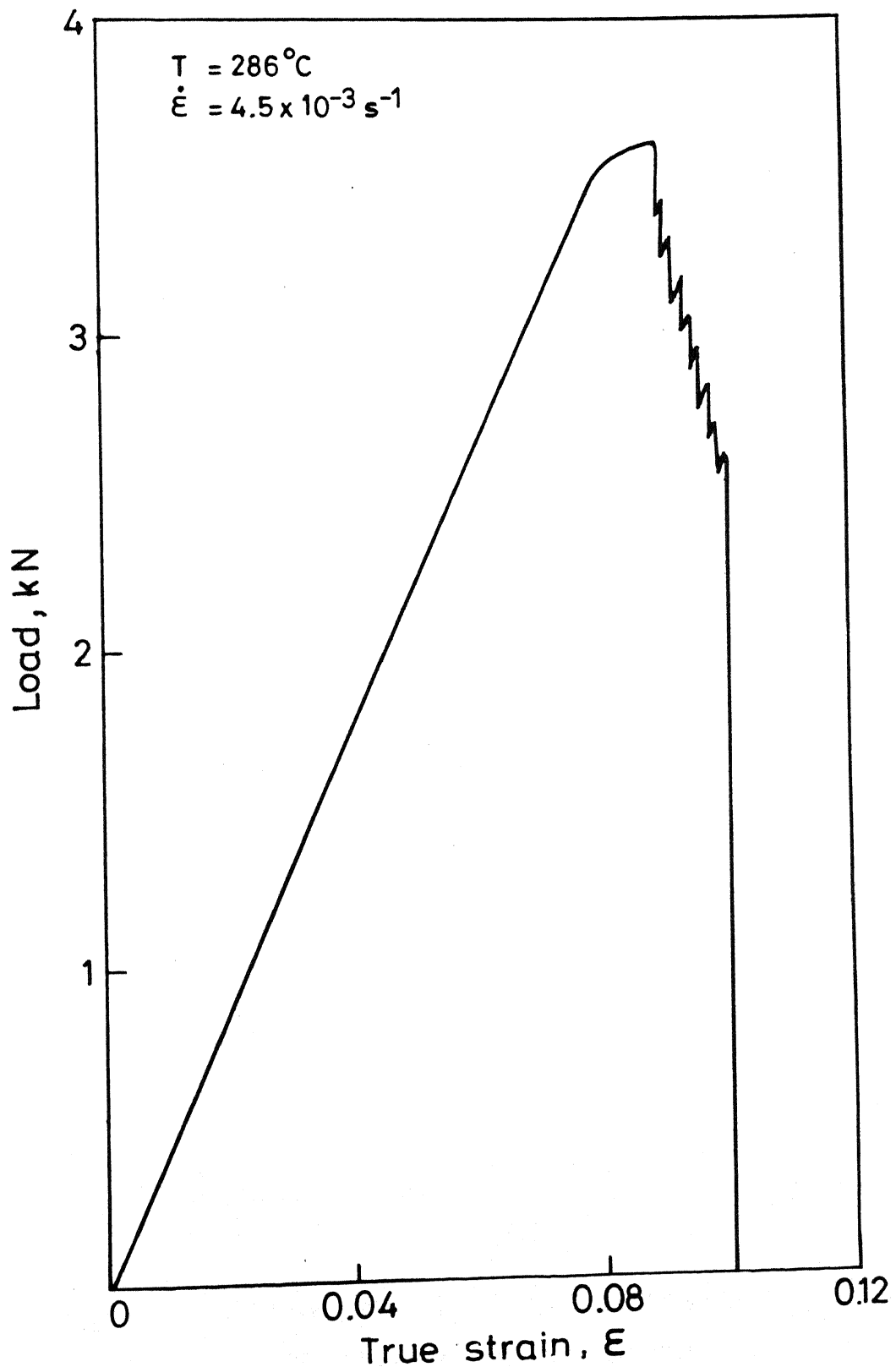


Fig. 4.09 Variation of load with elongation (TMT+DS).

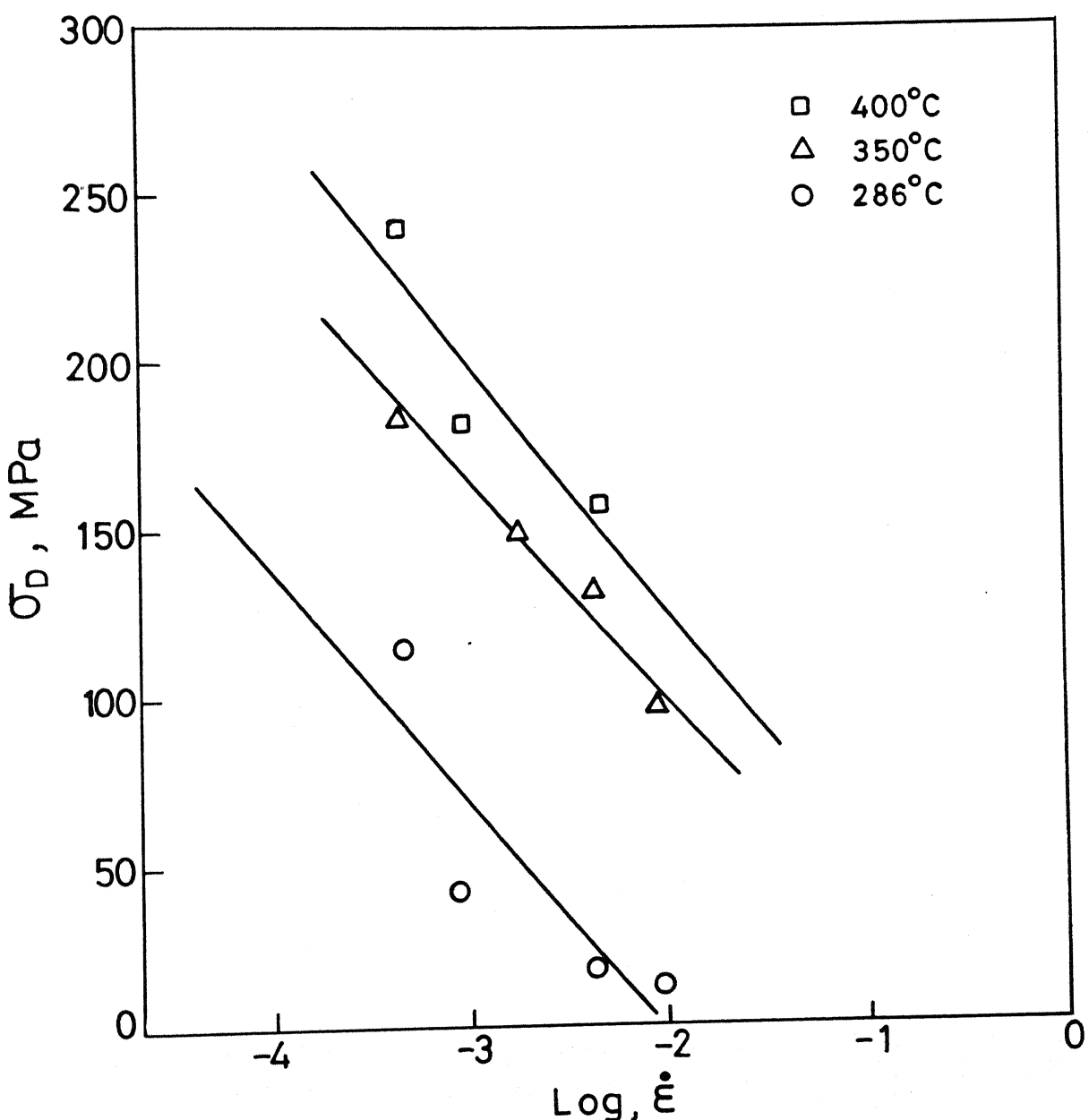


Fig. 4.10 Variation of stress decrement,  $\sigma_D$  at 9.4% strain as a function of strain rate,  $\dot{\epsilon}$  at different temperatures (TMT + DS)

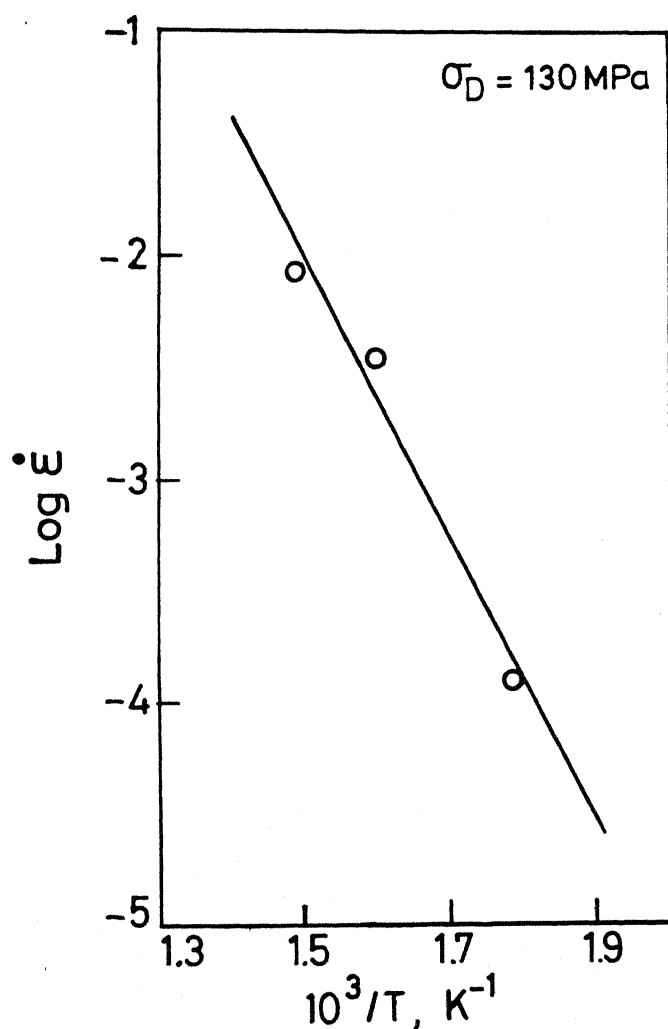


Fig. 4.11 Variation of strain rate,  $\dot{\epsilon}$ , as a function of temperature at constant stress decrement,  $\sigma_D$  (TMT + DS).

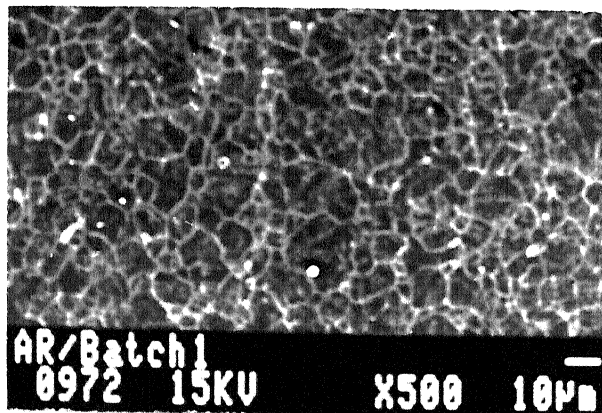


Fig. 4.12  
ARB1, M = 500X  
EE

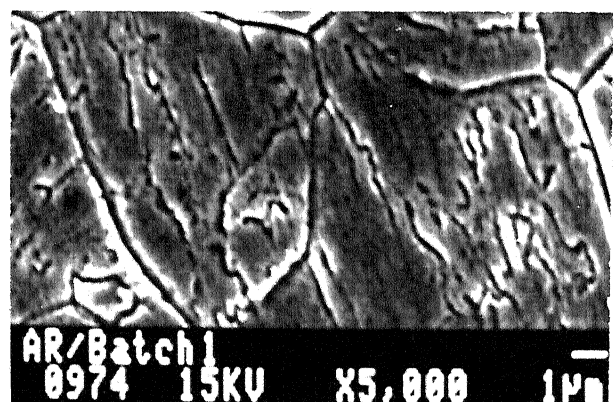


Fig. 4.13  
ARB1, M = 5000X  
EE

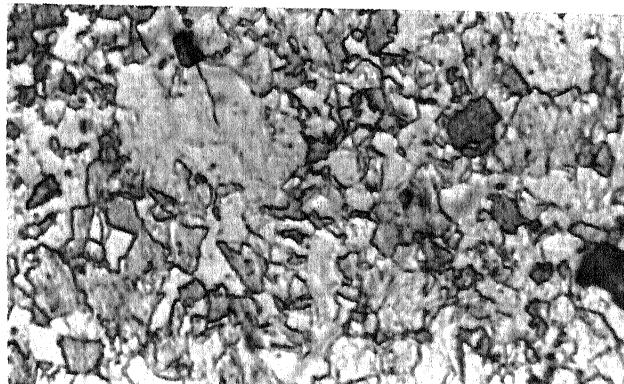


Fig. 4.14  
ARB1, M = 500X  
CE

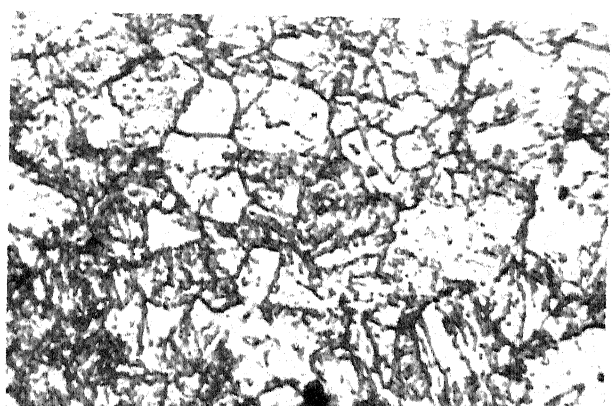


Fig. 4.15  
ARB1+SS, M = 500X  
EE

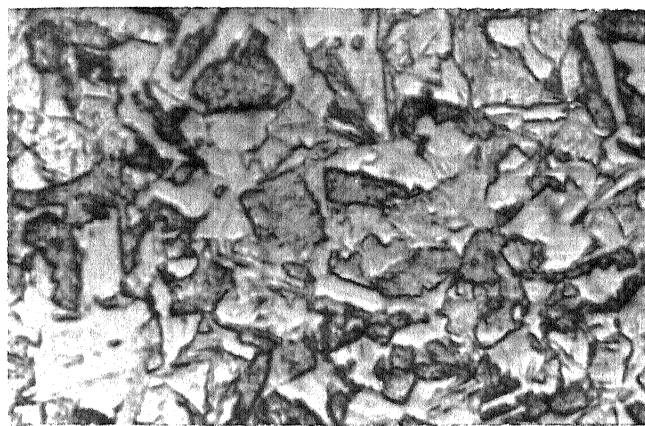


Fig. 4.16  
ARB1+SS, M = 500X  
CE

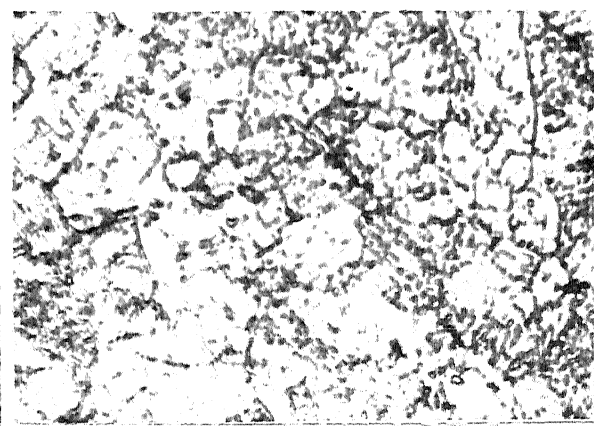


Fig. 4.17  
ARB1+DS, M = 500X  
EE

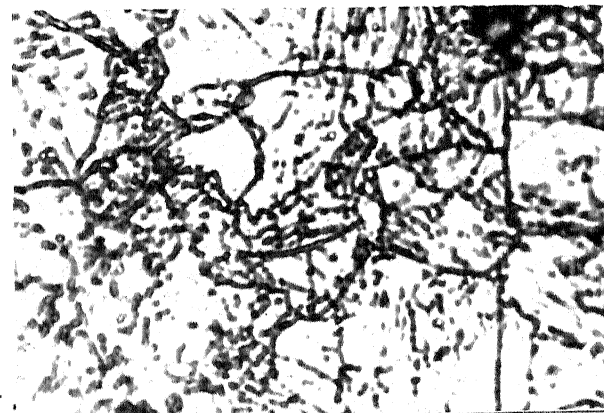


Fig. 4.18  
ARB1+DS, M = 1000X  
EE

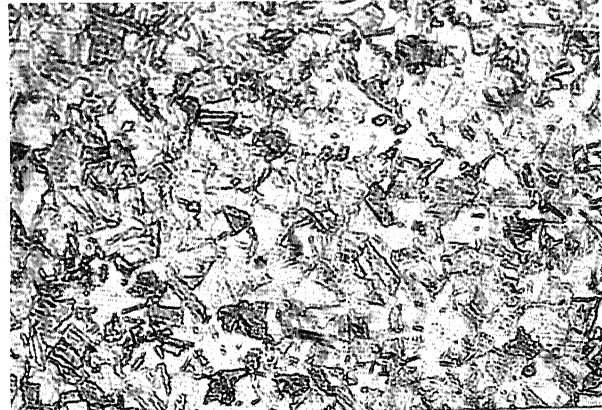


Fig. 4.19  
ARB1+DS, M = 200X  
CE

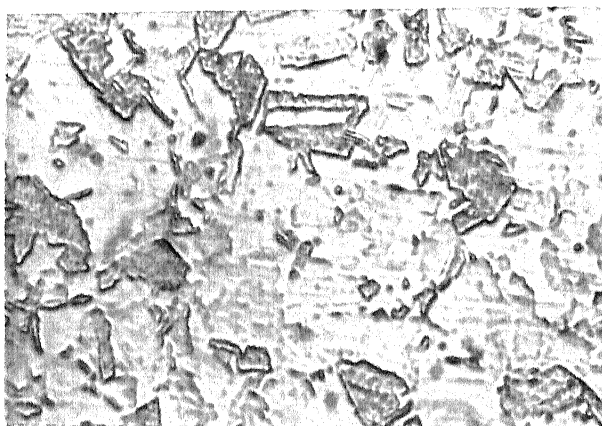


Fig. 4.2  
ARB1+DS, M = 500X  
CE

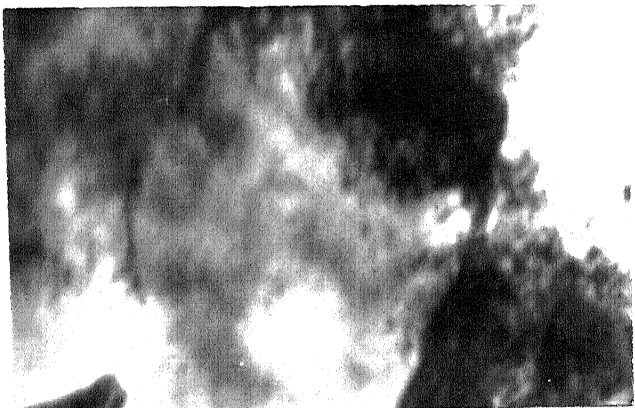


Fig. 4.21  
ARB1, M = 100,000X  
TEM

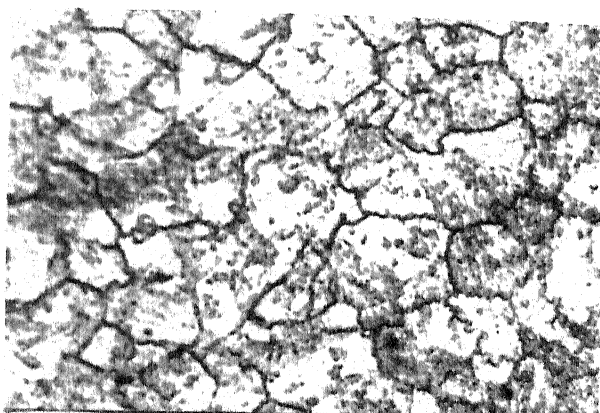


Fig. 4.22  
ARB2, M = 500X  
EE

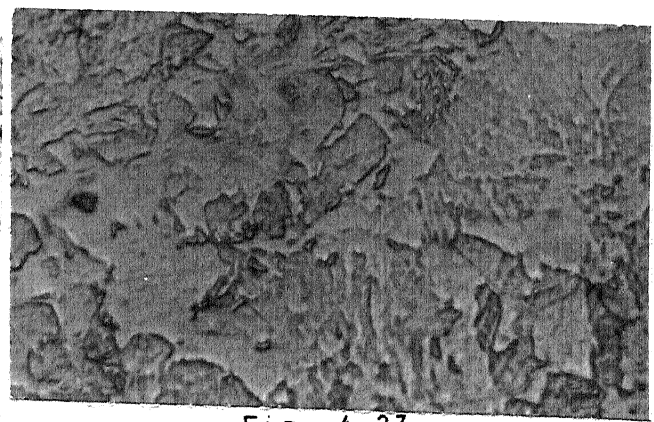


Fig. 4.23  
ARB2, M = 500X  
CE

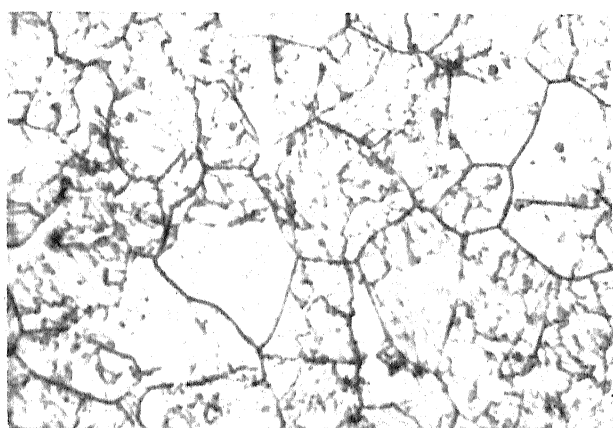


Fig. 4.24  
ARB2+SS, M = 500X  
EE

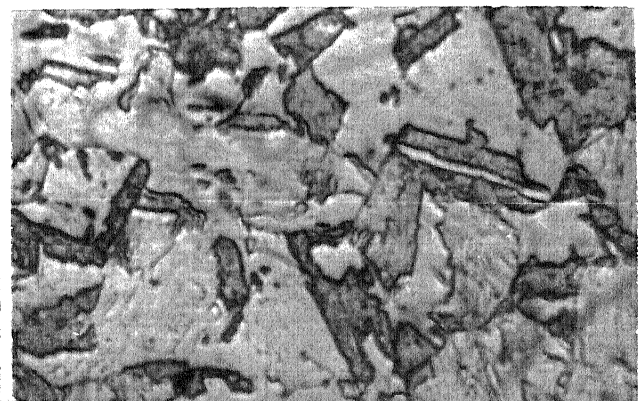


Fig. 4.25  
ARB2+SS, M = 500X  
CE

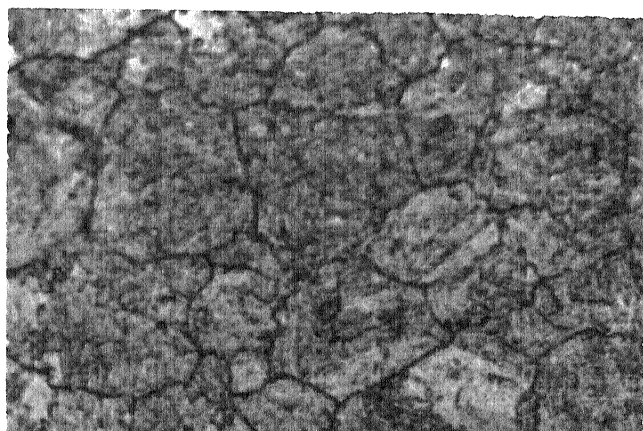


Fig. 4.26  
ARB2+DS, M = 500X  
EE

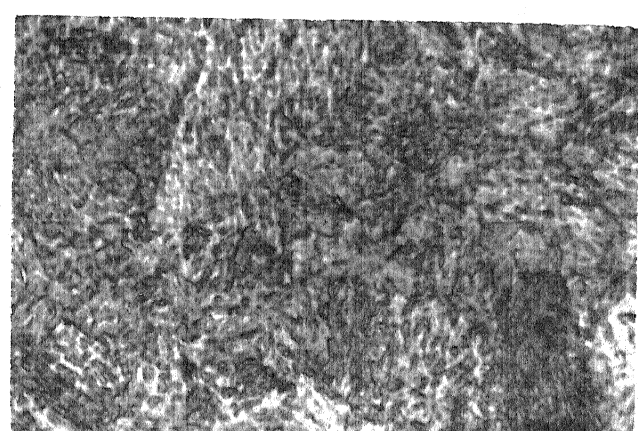


Fig. 4.27  
ARB2+DS, M = 500X  
CE

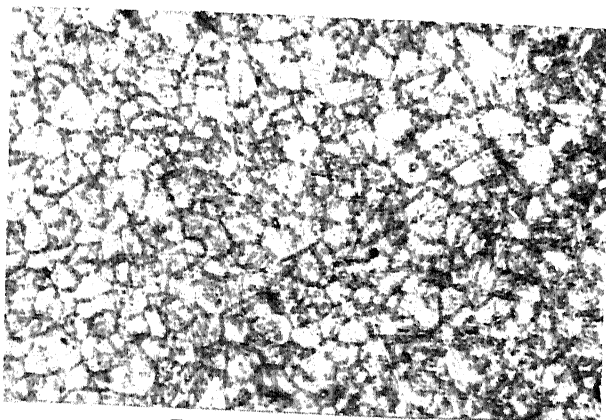


Fig. 4.28  
ARB2+TMT, M = 200X  
EE

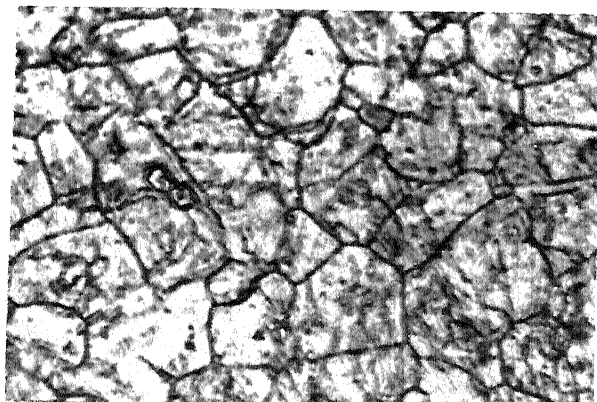


Fig. 4.29  
ARB2+TMT, M = 500X  
EE



Fig. 4.30  
ARB2+TMT, M = 1000X  
EE

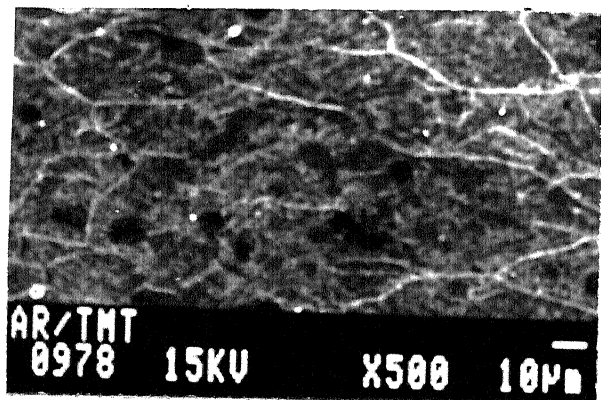


Fig. 4.31  
ARB2+TMT, M = 500X  
EE

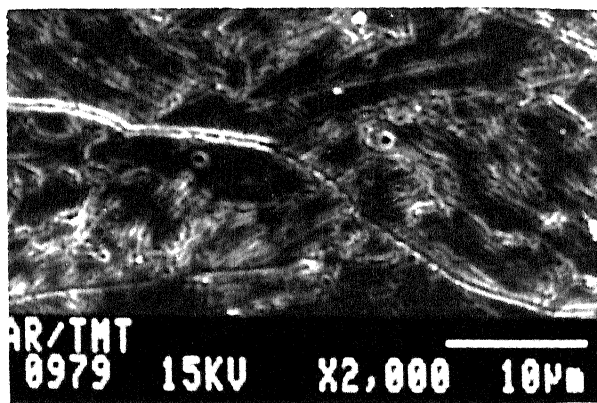


Fig. 4.32  
ARB2+TMT, M = 2000X  
EE

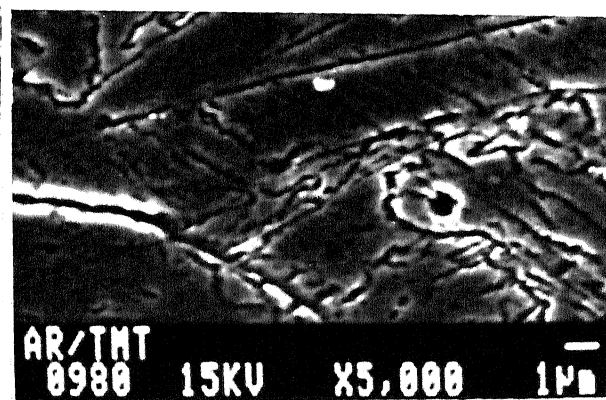


Fig. 4.33  
ARB2+TMT, M = 5000X  
EE



Fig. 4.34  
ARB2+TMT, M = 500X  
CE

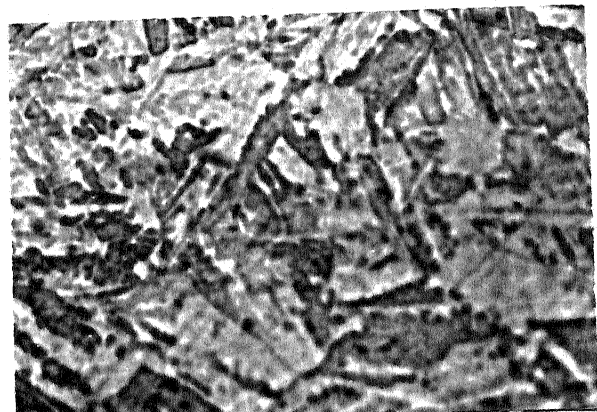


Fig. 4.35  
ARB2+TMT, M = 1000X  
CE

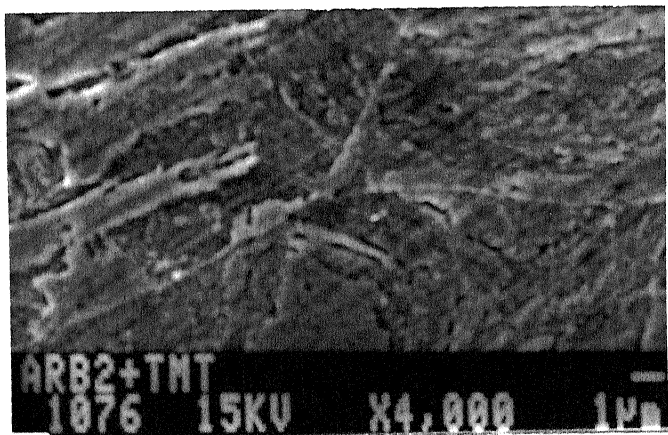


Fig. 4.36

ARB2+TMT, M = 4000X

CE

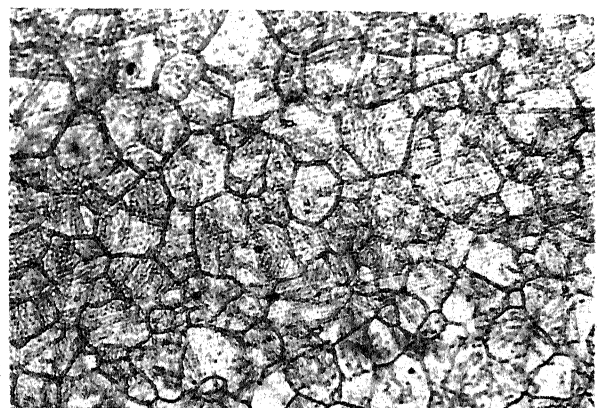


Fig. 4.37

ARB2+TMT+SS, M = 200X

EE

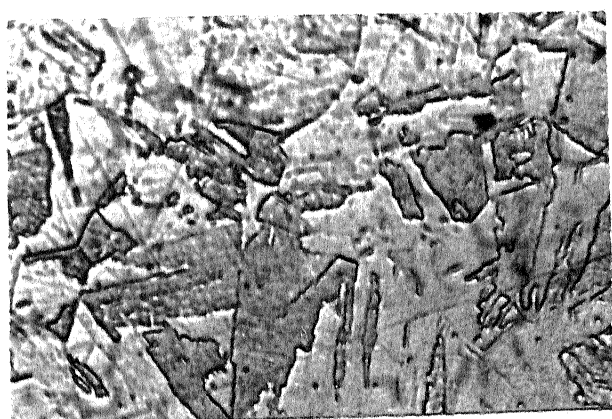


Fig. 4.38

ARB2+TMT+SS, M = 500X

CE



Fig. 4.39

ARB2+TMT+SS, M = 1000X

CE

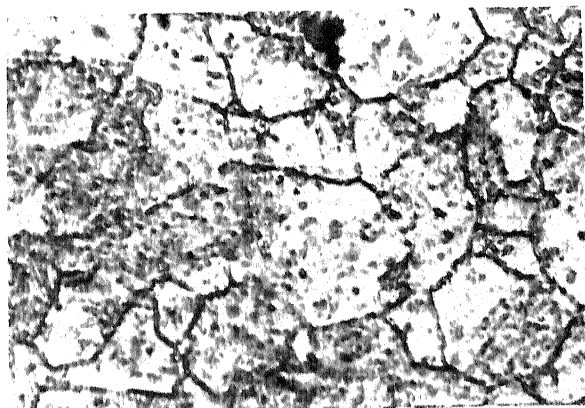


Fig. 4.40  
ARB2+TMT++DS, M = 500X  
EE

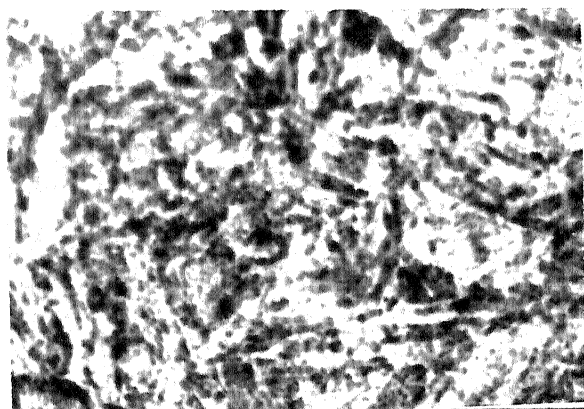


Fig. 4.41  
ARB2+TMT+DS, M = 500X  
CE

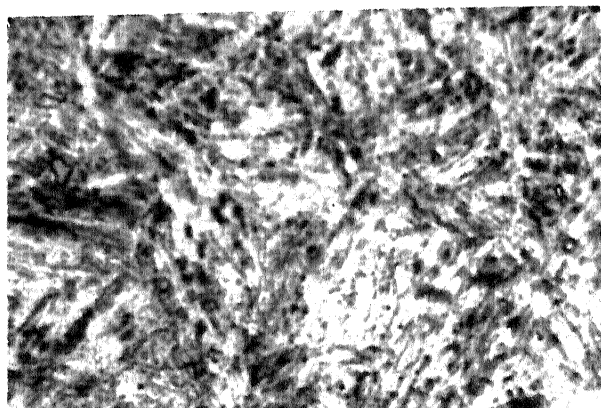


Fig. 4.42  
ARB2+TMT+DS, M = 1000X  
CE

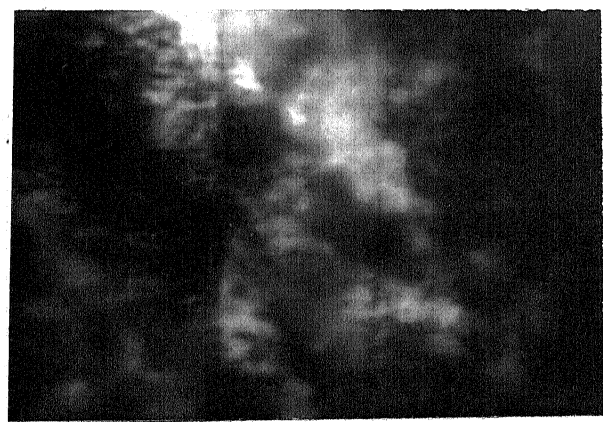


Fig. 4.43  
ARB2+TMT, M = 170,000X  
TEM

69

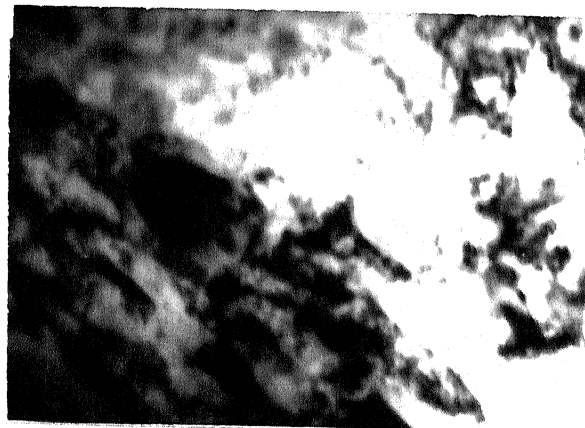


Fig. 4.44

ARB2+TMT+DS, M = 80,000X

TEM

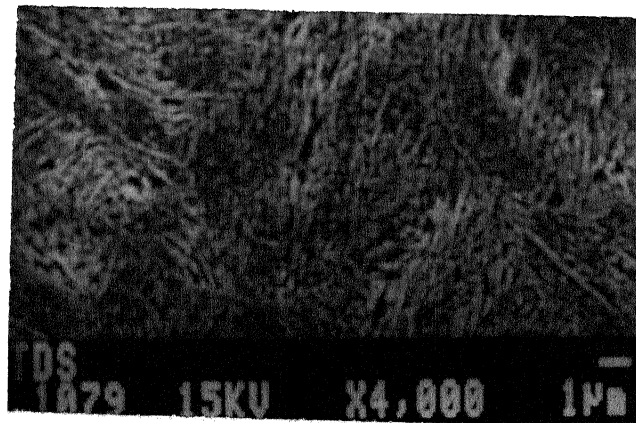


Fig. 4.45

ARB2+TMT+DS, M = 4000X

CE

TABLE 1.1

70

Nominal chemical composition and strengths of common maraging steels

Maraging steel type	Nominal composition, wt %*							Nominal yield strength (MPa)
	Ni	Co	Mo	Al	Ti	Cr	C(max)	
18 Ni 200	18	8.5	3.2	0.1	0.2	-	0.03	1378
18 Ni 250	18	8.0	4.8	0.1	0.4	-	0.03	1722
18 Ni 300	18.5	8.75	5.0	0.1	0.6	-	0.03	2067
12-5-3	12.0		3.0	0.4	0.2	5.0	0.03	1240
Cast 17 Ni	17.0	10.25	4.6	0.1	0.3	-	0.03	1619

\*Balance material in all the compositions is Fe.

TABLE 1.2

Steel			
Type of embrittlement	C and alloy steels	18 Ni 300 maraging	12-5-3 maraging
<u>HOT HYDROGEN</u>			
CVN after 1000 hrs at 454°C in 1000 psi H <sub>2</sub>	<13.35* J		42.72 J
<u>CATHODIC CHARGING HYDROGEN</u>			
Tensile Reduction of area after charging for 10 minutes at 0.02 amp/sq.inch in 4% H <sub>2</sub> SO <sub>4</sub> saturated by NaCN	3%*	42%	
Baking time at 149°C required to restore ductility of severely embrittled specimens	20 hrs*	2 hrs	
<u>NEUTRON RADIATION</u>			
Increase of transition temperature with $3 \times 10^{19}$ n/cm <sup>2</sup> (>1Mev) irradiation	121°C		20°C
<u>TEMPER</u>			
CVN after 10,000 hrs at 454°C	<13.35 J*		53.4 J

\* Quenched and aged.

TABLE 3.1

Maraging Steel type	Nominal Composition							C (Max)	Fe
	Ni	Co	Mo	Al	Ti	Cr			
18 Ni 250	18	8	4.8	.1	.4	-	.03	68.7	

TABLE 3.2

## ROLLING SCHEDULE

73

SPECIMEN THICKNESS (mm)		ROLLING TEMPERATURE (°C)	NO. OF PASSES	TOTAL REDUCTION (%)
INITIAL	FINAL			
4.8	3.17	1014	3	33.96
3.17	1.9	989	3	40.06
1.9	.86	957	3	54.55

TABLE 3.3  
TENSILE TEST PARAMETERS

74

Condition	Batch No.	Temperature of testing (°C)	Strain Rate, $\dot{\epsilon}$ (s <sup>-1</sup> )
ARB1+DS	1	286	$7.95 \times 10^{-5}$
			$1.59 \times 10^{-4}$
			$8.32 \times 10^{-4}$
		350	$4.07 \times 10^{-4}$
			$3.89 \times 10^{-3}$
			$8.91 \times 10^{-3}$
		400	$1.74 \times 10^{-3}$
			$3.98 \times 10^{-3}$
			$9.55 \times 10^{-3}$
ARB2+TMT+DS	2	286	$4.5 \times 10^{-4}$
			$8.59 \times 10^{-4}$
			$4.52 \times 10^{-3}$
		350	$9.12 \times 10^{-3}$
			$4.45 \times 10^{-4}$
			$1.77 \times 10^{-3}$
		400	$4.4 \times 10^{-3}$
			$8.85 \times 10^{-3}$
			$4.39 \times 10^{-4}$
			$9.15 \times 10^{-4}$
			$4.42 \times 10^{-3}$
			$8.9 \times 10^{-3}$

TABLE 3.4

75

Various Etchants and Their Chemical Composition Used for Metallographic Studies in 18% Ni Maraging Steel

Etch No.	Name of Etchant	Reagents
(a) For Matrix Structure (MS) and Grain Boundaries (GB)		
1.	Modified Ferric Chloride	$\text{FeCl}_3$ (0.5 g) + $\text{HNO}_3$ (10 ml) + HCl (20 ml) + dist. water (20 ml)
2.	Acetic Acid-Glycerol	Acetic acid (10%) + $\text{HNO}_3$ (10 ml) + HCl (15 ml) + Glycerine (65 ml)
3.	Vilella's reagent	Picric acid (1 g) + HCl (5 ml) + methanol (95%)
4.	Chromic Acid	Chromic acid 10% - electrolytic etching, 6V
(b) For Phases		
5.	Ferric Chloride	$\text{FeCl}_3$ (5 g) + HCl (10 ml) dist. water to make up 100 ml
6.	Picral	Picric acid (4 g) + HCl (2 ml) $\text{HNO}_3$ (2 ml) dist. water (100 ml) $\text{HNO}_3$ (3%) in methanol
7.	3% Nital	$\text{HNO}_3$ (1%) in methanol
8.	1% Nital	$\text{CuSO}_4$ (10g) + HCl (50 ml)
9.	Marble's reagent	+ dist. water (50 ml)

TABLE 4.01

T = 286°C

Condition = ARB2 + TMT + DS

$\sigma_D$ / 9.4% Strain (MPa)	$\dot{\epsilon}$ ( $s^{-1}$ )	log $\dot{\epsilon}$
114.47	$4.498 \times 10^{-4}$	-3.35
42.11	$8.5894 \times 10^{-4}$	-3.07
18.78	$4.5223 \times 10^{-3}$	-2.35
12.62	$9.1299 \times 10^{-3}$	-2.04

TABLE 4.02

 $T = 350^{\circ}\text{C}$ 

Condition = ARB2 + TMT + DS

$\sigma_D$ / 9.4% Strain (MPa)	$\dot{\epsilon} (\text{s}^{-1})$	$\log \dot{\epsilon}$
183.5	$4.447 \times 10^{-4}$	-3.35
149.46	$1.77 \times 10^{-3}$	-2.75
132.28	$4.3989 \times 10^{-3}$	-2.36
96.84	$8.8527 \times 10^{-3}$	-2.05

TABLE 4.03

T = 400°C

Condition = ARB2 + TMT + DS

$\sigma_D$ / 9.4% Strain (MPa)	$\dot{\epsilon}$ ( $s^{-1}$ )	log $\dot{\epsilon}$
241.21	$4.3885 \times 10^{-4}$	-3.36
183.64	$9.145 \times 10^{-4}$	-3.04
159.49	$4.4198 \times 10^{-3}$	-2.36

TABLE 4.04

AT  $\sigma_D = 130$  MPa

Condition = ARB2 + TMT + DS

Log $\dot{\epsilon}$ .	$\frac{1}{T} \times 10^3$
-3.9	1.79
-2.47	1.6
-2.07	1.49

TABLE 4.05

80

 $T = 286^{\circ}\text{C}$ 

XV = Cross head velocity (mm/min)

Condition = ARB1 + DS

$\sigma_D$ (MPa)	XV = .1	XV = .2	XV = 1
$\sigma_D$	132.64	98.19	81.73
$\epsilon_c$	.14	.11	.13

TABLE 4.06

 $T = 350^{\circ}\text{C}$ 

XV = Cross head velocity (mm/min)

Condition = ARB1 + DS

$\sigma_D$ (MPa)	XV = .5	XV = 5	XV = 10
$\sigma_D$	144.2	99.73	86.66
$\epsilon_c$	.13	.11	.14

TABLE 4.07

 $T = 400^{\circ}\text{C}$  $XV = \text{Cross head velocity (mm/min)}$ 

Condition = ARB1 + DS

$\sigma_D$ (MPa)	XV = 2	XV = 5	XV = 10
$\sigma_D$	176.42	126.46	120.97
$\epsilon_c$	.13	.13	.15

TABLE 4.08

AT  $\sigma_D = 130$  MPa

Condition = ARB1 + DS

Log $\dot{\epsilon}$ .	$\frac{1}{T} \times 10^3$
-4.23	1.79
-3.05	1.60
-2.27	1.49

TABLE 4.09

T = 286<sup>0</sup>C

Condition = ARB1 + DS

Log $\dot{\epsilon}$ .	$\sigma_D$ / 8.3% strain (MPa)
-4.0996	132.64
-3.7986	98.19
-3.0799	81.73

TABLE 4.10

 $T = 350^{\circ}\text{C}$ 

Condition = ARB1 + DS

Log $\dot{\epsilon}$ .	$\sigma_D$ / 8.3% strain (MPa)
-3.39	144.2
-2.41	99.73
-2.05	86.66

TABLE 4.11

T = 400°C

Condition = ARB1 + DS

Log $\dot{\epsilon}$ .	$\sigma_D$ / 8.3% strain (MPa)
-2.76	176.42
-2.4	126.47
-2.02	120.97

TABLE 4.12

Condition = ARB2 + TMT + DS

XV = 5 mm/min

$\sigma_D$ (MPa)	T = 286°C	T = 350°C	T = 400°C
$\sigma_{D_1}$	35.33	101.94	.47
$\sigma_{D_2}$			138.16
$\epsilon_{c_1}$	.09	.07	.02
$\epsilon_{c_1'}$			.07
$\epsilon_{c_2}$			.1

TABLE 4.13

Condition = ARB2 + TMT + DS

XV = 1 mm/min

$\sigma_D$ (MPa)	T = 286°C	T = 350°C	T = 400°C
$\sigma_{D_1}$	5.04		6.65
$\sigma_{D_2}$	34.19		183.64
$\sigma_{D_3}$	81.55		
$\epsilon_{c_1}$	.04		$8.34 \times 10^{-3}$
$\epsilon_{c_1}'$	.06		.13
$\epsilon_{c_2}$	.07		.13
$\epsilon_{c_2}'$	.09		
$\epsilon_{c_3}$	.13		

TABLE 4.14

Condition = ARB2 + TMT + DS

XV = .5 mm/min

$\sigma_D$ (MPa)	T = 286°C	T = 350°C	T = 400°C
$\sigma_{D_1}$	7.31	2.33	.99
$\sigma_{D_2}$	91.79	170.42	.99
$\sigma_{D_3}$			4.3
$\sigma_{D_4}$			248.07
$\epsilon_{c_1}$	.02	.01	$7 \times 10^{-3}$
$\epsilon_{c_1'}$	.03	.02	$8.59 \times 10^{-3}$
$\epsilon_{c_2}$	.09	.08	.02
$\epsilon_{c_2'}$			.03
$\epsilon_{c_3}$			.04
$\epsilon_{c_3'}$			.13
$\epsilon_{c_4}$			.14

TABLE 4.15

Condition = ARB2 + TMT + DS

XV = 10 mm/min

---

$\sigma_D$ (MPa)	T = 286°C	T = 350°C	T = 400°C
---------------------	-----------	-----------	-----------

TABLE 4.16

91

Condition = ARB2 + TMT + DS

T = 286°C

XV = Cross-head velocity (mm/min)

$\sigma_D$ (MPa)	XV = .5	XV = 1	XV = 5	XV = 10
$\sigma_{D_1}$	7.31	5.05	35.33	23.2
$\sigma_{D_2}$	91.79	34.19		
$\sigma_{D_3}$		81.55		
$\epsilon_{c_1}$	.02	.04	.09	.09
$\epsilon_{c_1'}$	.03	.06		
$\epsilon_{c_2}$	.09	.07		
$\epsilon_{c_2'}$		.09		
$\epsilon_{c_3}$		.13		

TABLE 4.17

92

Condition = ARB2 + TMT + DS

T = 350°C

XV = Cross-head velocity (mm/min)

$\sigma_D$ (MPa)	XV = .5	XV = 2	XV = 5	XV = 10
$\sigma_{D_1}$	2.33	152.87	101.94	90.26
$\sigma_{D_2}$	170.42			
$\epsilon_{c_1}$	.01	.09	.07	.08
$\epsilon_{c_1}'$	.02			
$\epsilon_{c_2}$	.08			

TABLE 4.18

Condition = ARB2 + TMT + DS

 $T = 400^{\circ}\text{C}$ 

XV = Cross-head velocity (mm/min)

$\sigma_D$ (MPa)	XV = .5	XV = 1	XV = 5	XV = 10
$\sigma_{D_1}$	.99	6.65	.47	159.27
$\sigma_{D_2}$	.99	183.64	138.16	
$\sigma_{D_3}$	4.3			
$\sigma_{D_4}$	248.07			
$\epsilon_{c_1}'$	$7 \times 10^{-3}$	$8.34 \times 10^{-3}$	.02	.09
$\epsilon_{c_1}''$	$8.59 \times 10^{-3}$	.12	.07	
$\epsilon_{c_2}'$	.02	.13	.1	
$\epsilon_{c_2}''$	.03			
$\epsilon_{c_3}'$	.04			
$\epsilon_{c_3}''$	.12			
$\epsilon_{c_4}'$	.13			

TABLE 4.19

Condition	Grain size( $\mu\text{m}$ )	Aspect Ratio
ARB1	8.95	
ARB1 + SS	12.5	
ARB1 + DS	14.2	
ARB2	26.33	
ARB2 + SS	28	
ARB2 + DS	29	
ARB2 + TMT		2.3
ARB2 + TMT + SS	33	
ARB2 + TMT + DS	35	

## CHAPTER 5

## CONCLUSIONS AND SUGGESTIONS FOR FURTHER WORK

## 5.1 Conclusions :

- (i) Serrated yielding in 18 Ni 250 maraging steels, was observed in the temperature range of 286 to 400°C and in the strain rate range of  $7.95 \times 10^{-5}$  to  $9.55 \times 10^{-3}$  s<sup>-1</sup>.
- (ii) The serrations were accompanied by an audible acoustic emission.
- (iii) Multistaged serrated yielding was observed in thermomechanically treated specimens in the above mentioned temperature and strain rate regimes. On the other hand double solutionized samples showed only one stage of serrated yielding.
- (iv) The activation energy for "thermomechanically treated + double solutionized specimens" in the final stage of serrations was similar to that of single and double solutionized specimens.
- (v) The physical process underlying serrated yielding cannot be pinpointed at this stage. The existing models do not satisfactorily explain all the manifestations of dynamic strain aging. Perhaps a more refined analysis involving interaction energy, acoustic emission and transmission electron microscopy would provide a better basis for comparison of the competing models.
- (vi) The microstructural observation seem to indicate no grain refinement due to thermomechanical treatment. But transmission electron micrographs and scanning electron micrographs indicate a refining of blocks/laths. This refinement at block/lath level could lead to superior mechanical properties since the block is

the basic microstructural unit controlling the strength and fracture of 18 Ni 250 maraging steels. It is suggested that the superior mechanical properties reported for double solutionized [2] specimens could be due to refinement at the block/lath level.

#### 5.2 Suggestions for further work :

Transmission electron microscopy of dynamically aged specimens could shed further light on the phenomenon of dynamic strain aging. It would be a worthwhile idea to study the dynamic strain aging behaviour of irradiated specimens of 18 Ni 250 maraging steel because maraging steels are extensively used in the nuclear industry where radiation damage is a problem of serious concern.

Acoustic emission measurements could be carried out to examine the shock wave dynamics operating during twinning.

## REFERENCES

97

1. B.Z. Weiss, "Speciality Steels and Hard Materials", Proc. of the International Conference on Recent Developments in Speciality Steels and Hard Materials (edited by N.R. Comins and J.B. Clark) p.35, Pergamon Press (1982).
2. R.F. Decker, C.J. Novak and T.W. Landig, Journal of Metals, 11, 60 (1967).
3. S. Floreen, Met. Reviews, 13, 115 (1968).
4. F.W. Zones and W.I. Pumphrey, Jour. Iron Steel Inst., 163, 121 (1949).
5. J.M. Marder and A.R. Marder, Trans. ASM, 62, 1 (1969).
6. T. Maki, K. Tsuzaki and I. Tamura, Tetsu-to-Hagané, 65, 515 (1979).
7. V.D. Sadovskiy, V.M. Schastlivtsev, Yu.V. Kaletina and I.L. Yakoleva, Phys. Met. Metallog., 62, 190 (1986).
8. C. Servant and G. Cizeron, Mém. Sci. Rev. Mét., 66, 531 (1969).
9. K. Hosomi, Y. Ashida, H. Hato and K. Ishihara, Tetsu-to-Hagané, 61, 1012 (1975).
10. T. Fujita, K. Asami, S. Yamamoto and H. Tutumi, Tetsu-to-Hagané, 56, 214 (1970).
11. V.D. Sadovskiy, Phys. Met. Metallog., 57, 1 (1984).
12. G. Krauss and M. Cohen, Trans. AIME, 224, 1212 (1962).
13. T.J. Koppenaal and E. Gold, Met. Trans. 3, 2965 (1972).
14. G.P. Miller and W.I. Mitchell, Jour. Iron Steel Inst., 203, 899 (1965).

15. J.M. Chilton and C.J. Barton, Trans. ASM, 60, 528 (1967).
16. S.K. Das and G. Thomas, Trans. ASM, 62, 659 (1969).
17. R.D. Garwood and R.D. Jones, Jour. Iron Steel Inst., 204, 512 (1966).
18. S. Takaki and Y. Tokunaga, Trans. JIM, 23, 31 (1982).
19. A.F. Yedneral, O.P. Zhukov, M.A. Kablukovskaya, B.M. Mogutnov and M.D. Perkas, Phys. Met. Metallog., 36, 46 (1973).
20. D.T. Peters and C.R. Cupp, Trans. Met. Soc. AIME, 236, 1420 (1966).
21. J.M. Genin and G. LeCaer, Scripta Met., 8, 15 (1974).
22. C. Servant, G. Maeder and G. Cizeron, Met. Trans., 6A, 981 (1981).
23. Y. Tokunaga and M. Morishige, J. Japan Inst. Metls., 43, 834 (1979).
24. H. Ohtani, F. Teraski and T. Kunitake, Tetsu-to-Hagané, 58, 434 (1972).
25. A.R. Harder and G. Krauss, Trans. ASM, 62, 957 (1969).
26. M.J. Roberts, Met. Trans., 1, 3287 (1970).
27. T. Swarr and G. Krauss, Met. Trans., 7A, 41 (1976).
28. L.-Å. Norström, Scand. J. Met., 5, 41 (1976).
29. K. Hosumi, Y. Ashida, H. Hato and K. Ishihara, Tetsu-to-Hagané, 64, 1047 (1978).
30. L.-Å. Norström, Metal Sci. J., 10, 429 (1976).
31. S. Matsuda, T. Inoue, H. Mimura and Y. Okamoto, Proc. of Inter. Sympo. on Toward Improved Ductility and Toughness, Climax Molybdenum Development Co. (Japan) Ltd., 47 (1971).

32. W.S. Owen, Proc. of 2nd Inter. Conf. on Strength of Metals and Alloys, III, Asilomar, 795 (1970).
33. Y. Kawabe, K. Nakazawa and S. Muneki, Trans. Nat. Research Inst. Metals, 20, 229 (1978).
34. S. Muneki, Y. Kawabe and K. Nakazawa, Tetsu-to-Hagané, 64, 605 (1978).
35. R.W. Hayes, Materials Science and Technology, 1, 285 (1985).
36. P. Rodriguez, Bulletin of Materials Science, 6, 653 (1984).
37. J.C. Fisher, Acta Metall, 2, 9 (1954).
38. G. Schoeck and A. Seeger, Acta Metall, 7, 469 (1959).
39. S.L. Mannan and P. Rodriguez, Phil. Mag, 25, 673 (1972).
40. G.E. Dieter, "Mechanical Metallurgy", Third Edition, pp 284-297, McGraw-Hill Book Company, (1986).
41. R.W. Hayes and W.C. Hayes, Acta Metall., 30, 1295 (1982).
42. R.W. Hayes, Acta Metall., 31, 365 (1983).
43. R.W. Hayes and W.C. Hayes, Acta Metall., 32, 259 (1984).
44. L.P. Kubin and Y. Estrin, Acta Metall. Mater., 38, 697 (1990).
45. A. Van den Beukel, Physica Status Solidi(a) 30, 197 (1975).
46. D.M. Barnett, W.C. Oliver and W.C. Nix, Acta Metall., 30, 673 (1982).
47. A.H. Cottrell, "Dislocations and plastic flow in crystals", pp.147-149, Clarendon Press, Oxford, (1953).
48. P.G. McCormick, Acta Metall., 36, 3061 (1988).
49. W. Räuchle, O. Vöhringer and E. Macherauch, Mater. Sci. Engng, 12, 147 (1973).
50. H. Conrad and H. Weidersich, Acta Metall., 8, 128 (1960).
51. Z.S. Basinski, Acta Metall., 5, 684 (1957).

52. T. Nakada and A.S. Keh, *Acta Metall.*, 18, 437 (1970).
53. R.A. Mulford and U.F. Kocks, *Acta Metall.*, 27, 1125 (1979).
54. S.G. Harris, "Vacancies and other point defects in metals and alloys", (1st Edn), pp 220-221, Bungay, Suffolk, Richard Clay and Co. (1958).

## APPENDIX 1

**Activation energy for deformation of metals at low temperatures :**

It is now generally accepted that in many cases deformation of metals is governed by thermally activated processes. If a single activation process is the controlling mechanism for the deformation, the strain rate ( $\dot{\epsilon}$ ) can be expressed by [50]

$$\dot{\epsilon} = A \exp \left( -\frac{\Delta G}{RT} \right) \quad (A1)$$

$$= A \exp (\Delta S/R) \exp(-\Delta H/RT) \quad (A2)$$

where A is effectively the product of the rate at which attempts to overcome the barrier are made and the strain produced by a successful fluctuation,  $\Delta G$  is the change in Gibbs free energy of the system,  $\Delta H$  is the enthalpy of activation (commonly termed "activation energy") and  $\Delta S$  is the change in entropy of the system. A,  $\Delta G$ ,  $\Delta H$  and  $\Delta S$  will generally depend upon stress, temperature and structure [50]. Only if certain simplifying assumptions are made can values for  $\Delta H$  be derived from experimental data.

Basinski [51] made the following assumptions :

- (i) A and  $\Delta S$  are independent of stress and temperature
- (ii) to a first approximation  $\Delta H$  is a constant for a constant ratio of applied stress,  $\sigma$  to the shear modulus,  $\mu$  at any strain i.e.  $H = H(\sigma/\mu)$ .

But experimental evidence indicates that

$$H = H(\bar{\sigma}) \quad (A3)$$

where  $\bar{\sigma}$  is the effective stress.  $\bar{\sigma}$  can be expressed as

$$\bar{\sigma} = \sigma - \sigma_\mu \quad (A4)$$

where  $\sigma_\mu$  is the long range internal stress field at any given structure.

Based on assumption (i) and equation (A3), Hayes [41] derived an expression for activation energy as follows

$$\dot{\epsilon} = A \exp(\Delta S/R) \exp(-\Delta H/RT) \quad (A2)$$

$$= \psi \exp(-\Delta H/RT) \quad (A5)$$

where  $\psi$  is given by the following expression

$$\psi = A \exp(\Delta S/R)$$

$$\ln \frac{\dot{\epsilon}}{\psi} = - \frac{\Delta H}{RT} \quad (A6)$$

$$\frac{\partial \ln \frac{\dot{\epsilon}}{\psi}}{\partial \left( \frac{1}{T} \right)} = - \frac{\Delta H}{R} \quad (A7)$$

$$-\Delta H = \frac{R \partial \ln \frac{\dot{\epsilon}}{\psi}}{\partial \left( \frac{1}{T} \right)} \quad (A8)$$

$$-\Delta H = \frac{R \partial \ln \dot{\epsilon}}{\partial \left( \frac{1}{T} \right)} \quad (A9)$$

$$-\Delta H = \frac{R \partial [2.3026 \log \dot{\epsilon}]}{\partial \left( \frac{1}{T} \right)} \quad (A10)$$

$$\Delta H = -2.3026 R \frac{\partial (\log \dot{\epsilon})}{\partial \left( \frac{1}{T} \right)} \quad (A11)$$

$$\Delta H = - \frac{R}{\log e} \frac{\partial (\log \dot{\epsilon})}{\partial \left( \frac{1}{T} \right)} \quad (A12)$$

$$\Delta H = \frac{-R \times 10^3}{\log e} \cdot \frac{\partial (\log e)}{\partial \left( \frac{1}{T} \times 10^3 \right)} \quad (A13)$$

Let slope of  $\log e$  vs  $\frac{1}{T} \times 10^3$  be  $m_1$ . Hence

$$m_1 = \frac{-\Delta H \log e}{R \times 10^3} \quad (A14)$$

**Significance of stress decrement :**

Stress decrement,  $\sigma_D$  is defined as the stress differential between the breakaway stress at which dislocations escape from their atmosphere and the stress at which they move easily through the lattice before being pinned again [41, 42]. In terms of stress-strain curve,  $\sigma_D$  is simply the height of the individual serrations.

The bulk of the prior work in strain ageing has concentrated on the critical strain ( $\epsilon_c$ ) as the criterion for studying strain ageing. However, complications arise in using  $\epsilon_c$  and it appears as though the  $\epsilon_c$  criterion is only suitable for very simple alloy systems. Even then, this criterion may be limited to the lower temperature portion of the strain ageing region. For example, Nakada and Keh [52] show a reversal of the critical strain vs. temperature curve above 200°C for high purity Ni-C alloys. Also, Mulford and Kochs [53] discuss the ambiguous role of  $\epsilon_c$  in Inconel 600. Finally, Harris [54] reported the reversal of the  $\epsilon_c$  vs temperature curves for aging Aluminium alloys.

In contrast, studies (including the present one) showed no anomalous behaviour of stress decrement ( $\sigma_D$ ) measurement throughout the entire temperature regime for a complex alloy. Hence Hayes [41-43] suggested that stress decrement may be a more fundamental measurement of strain ageing than is the critical strain.

AAJJ2493

ME-1991-M-SUN-EFF